Contents lists available at ScienceDirect

ISPRS Journal of Photogrammetry and Remote Sensing

journal homepage: http://ees.elsevier.com

Burn severity analysis in Mediterranean forests using maximum entropy model trained with EO-1 Hyperion and LiDAR data

Alfonso Fernandez-Manso[a,b], Carmen Quintano[b,c,d,*], Dar A. Roberts[b]

[a] Agrarian Science and Engineering Department, University of León, Av. Astorga s/n, 24400 Ponferrada, Spain
[b] Department of Geography, University of California, Santa Barbara, CA 93106, United States
[c] Electronic Technology Department, University of Valladolid, C/ Francisco Mendizábal, s/n, 47014 Valladolid, Spain
[d] Sustainable Forest Management Research Institute, University of Valladolid-Spanish National Institute for Agricultural and Food Research and Technology, Spain

ARTICLE INFO

Keywords
Burn severity
EO-1 Hyperion
LiDAR
MaxEnt

ABSTRACT

All ecosystems and in particular ecosystems in Mediterranean climates are affected by fires. Knowledge of the drivers that most influence burn severity patterns as well an accurate map of post-fire effects are key tools for forest managers in order to plan an adequate post-fire response. Remote sensing data are becoming an indispensable instrument to reach both objectives. This work explores the relative influence of pre-fire vegetation structure and topography on burn severity compared to the impact of post-fire damage level, and evaluates the utility of the Maximum Entropy (MaxEnt) classifier trained with post-fire EO-1 Hyperion data and pre-fire LiDAR to model three levels of burn severity at high accuracy. We analyzed a large fire in central-eastern Spain, which occurred on 16–19 June 2016 in a maquis shrubland and *Pinus halepensis* forested area. Post-fire hyperspectral Hyperion data were unmixed using Multiple Endmember Spectral Mixture Analysis (MESMA) and five fraction images were generated: char, green vegetation (GV), non-photosynthetic vegetation, soil (NPVS) and shade. Metrics associated with vegetation structure were calculated from pre-fire LiDAR. Post-fire MESMA char fraction image, pre-fire structural metrics and topographic variables acted as inputs to MaxEnt, which built a model and generated as output a suitability surface for each burn severity level. The percentage of contribution of the different biophysical variables to the MaxEnt model depended on the burn severity level (LiDAR-derived metrics had a greater contribution at the low burn severity level), but MaxEnt identified the char fraction image as the highest contributor to the model for all three burn severity levels. The present study demonstrates the validity of MaxEnt as one-class classifier to model burn severity accurately in Mediterranean countries, when trained with post-fire hyperspectral Hyperion data and pre-fire LiDAR.

1. Introduction

Fires burn forests, agricultural land and natural areas each year in almost all terrestrial ecosystems, with important ecological and biophysical repercussions (Bowman et al., 2009; Scott et al., 2013). According to the Joint Research Centre (JRC) of the European Commission more than 700,000 ha burned in the European Union in 2017 and many human lives were lost (San-Miguel-Ayanz et al., 2016). Moreover, due to climate change, extreme weather conditions (heat waves, drought, strong winds) may have an impact on many of Europe's forests with more frequency and higher severity, easing the ignition, propagation and intensity of fires (San-Miguel-Ayanz et al., 2016). An appropriate natural resource management is crucial to reduce forest fire risk and severity (Frolking et al., 2009). Furthermore, a post-fire management approach that preserves post-fire vegetation and soils can only be based on accurate monitoring of fire effects (Brewer, 2016; Lentile et al., 2006). Burned area and burn severity are the two most commonly used metrics for evaluating fire effects (Meng and Zhao, 2017). The distinction between the terms burn severity and fire severity has been discussed previously (Keeley, 2009). According to Jain et al. (2004), burn severity includes short and long-term effects of fire, referring to what is left after fire. Field-based monitoring of both burned area and burn severity, although essential, is costly in time and resources. For that reason, remote sensing-based assessment is now widely used. Examples include the Monitoring Trends in Burn Severity (MTBS, https://www.mtbs.gov) Project in the USA, or the European Forest Fire Information System (EFFIS, http://effis.jrc.ec.europa.eu)

* Corresponding author at: Department of Electronic Technology, University of Valladolid, C/ Paseo del Cauce, 59, 47011 Valladolid, Spain.
Email address: carmen.quintano@uva.es (C. Quintano)

https://doi.org/10.1016/j.isprsjprs.2019.07.003
Received 26 March 2019; Received in revised form 3 July 2019; Accepted 4 July 2019
Available online xxx
0924-2716/

and many research studies (Chen et al., 2015b; Fernández-García et al., 2018; Huang et al., 2013; Pleniou et al., 2013; Quintano et al., 2018; among others). A substantial number of these studies are based on spectral indices that condense the spectral changes caused by burning into a single response variable (e.g. Fernández-Manso et al., 2016a; Lu et al., 2015; Stroppiana et al., 2012). The Normalized Burn Ratio (NBR, Key and Benson, 2006), in particular, its differenced version (dNBR, Key and Benson, 2006) or relativized versions (RdNBR, Miller and Thode, 2007), have become a standard means to assess burn severity from satellite data (see Fernández-García et al., 2018; Lhermitte et al., 2011; McCarley et al., 2017, among others).

Usually, the short-term post-fire scene is a combination of vegetation, soil and ash. For this reason, studying fire effects may basically be regarded as a sub-pixel question (Quintano et al., 2013). Consequently, spectral mixture analysis (SMA, Shimabukuro and Smith, 1991), one the most widely used sub-pixel techniques, has been successfully employed for post-fire assessment by many researchers (e.g. Fernández-Manso et al., 2009, 2016b; Lentile et al., 2009; Veraverbeke et al., 2014). SMA, however, only allows one spectrum for endmember class, therefore the variability in the scene (different spectral responses could correspond to a same material) can not be incorporated in the model. Multiple Endmember SMA (MESMA, Roberts et al., 1998) overcomes this limitation by enabling multiple spectra for each endmember class, thus accounting for within class spectral variability. MESMA has demonstrated its effectiveness for a wide variety of remote sensing applications: mapping coal mining affected areas (Fernández-Manso et al., 2012), plant species (Lippitt et al., 2017; Hamada et al., 2011), invasive species (Amaral et al., 2015), urban materials (Wetherley et al., 2017), wetland vegetation (Michishita et al., 2012), or biomass (Swatantran et al., 2011) as some examples. MESMA has also been successfully employed for post-fire monitoring, mainly through the char fraction image (Dennison et al., 2006; Fernández-Manso et al., 2016b; Quintano et al., 2013, 2017; Veraverbeke et al., 2012, 2014). Moreover, recent studies (Tane et al., 2018; Veraverbeke and Hook, 2013; Veraverbeke et al., 2014) have verified the high correlation between field measured burn severity (usually using CBI) and MESMA fraction images.

Although both SMA and MESMA can unmix broadband multispectral remotely sensed data like Landsat, a higher sensitivity may be obtained when using narrowband hyperspectral data, as shown by Veraverbeke et al. (2014) and Tane et al. (2018) using data from the Airborne Visible/Infrared Imaging Spectrometer (AVIRIS: Green et al., 1998). Airborne imagery, mainly from AVIRIS, have been employed in many hyperspectral fire studies (Tane et al. 2018; van Wagtendonk et al., 2004; Veraverbeke et al., 2014). Hyperion (Pearlman et al., 2003) onboard of the Earth-Observing One (EO-1) platform is the only spaceborne hyperspectral sensor to date that recorded data from approximately 0.4 to 2.5 μm, wavelengths that has proven its usefulness in monitoring fire effects. Our burn severity study is based on MESMA fraction images from Hyperion data, in particular, on the char fraction image that has shown a strong relationship to burn severity (Fernández-Manso et al., 2009; Sunderman and Weisberg, 2011; Tane et al., 2018; Veraverbeke and Hook, 2013). Spectral indices are based exclusively on the spectral information contained in two or three spectral bands. They do not fully profit from the whole spectral information available in hyperspectral data (Veraverbeke et al., 2018). In addition, MESMA fraction images have a physical meaning; they represent the quantitative abundance of the ground cover classes (Quintano et al., 2012) and do not need to be calibrated with field data as spectral indices do (Somers et al., 2010).

Pre-fire forest structure is an important factor in fire severity (Agee, 1997; Agee and Skinner, 2005). Several studies have related vegetation structural parameters measured from ground plots, such as plant canopy cover, tree density and size and fine fuel accumulations, to burn severity (Kuenzi et al., 2008; Lentile et al., 2006). However, passive satellite sensors have limitations in detecting fuel spatial complexity due to their incapacity to penetrate the forest canopy (Keane et al., 2001). Fine resolution LiDAR data are commonly used to estimate forest structure and terrain elevation (Cao et al., 2019; Liu et al., 2018). They are composed of point clouds that register the spatial location where a pulse of laser light meets an object. When different layers of vegetation are present, a pulse can result in different points of the cloud (Wulder et al., 2012). Vegetation can be characterized vertically and horizontally by LIDAR data enabling the determination of the shapes of individual trees and shrubs (Price and Gordon, 2016). Thus, LiDAR data allow for characterizing stand structure and mapping fuel loads or biomass (Chen et al., 2017; Kramer et al., 2014; Liu et al., 2018; Price and Gordon, 2016; Stavros et al., 2018, Tsui et al., 2012). García-Llamas et al. (2019) in their study about environmental drivers of burn severity related a structural parameter from LiDAR (i.e., the CV of vegetation heights) to burn severity in fire-prone pine ecosystems. Their results indicated the applicability of using pre-fire vegetation structure measurements from LiDAR data for predicting burn severity, as a valid complement to spectral satellite measurements. Based on this study, our hypothesis is that characterizing pre-fire forest structure from fine spatial resolution LiDAR data could potentially complement the information of the MESMA Hyperion post-fire char fraction image about burn severity. Some studies have already combined multispectral/hyperspectral data and LiDAR data to map fuel types (Erdody and Moskal, 2010; Marino et al., 2016; Mutlu et al., 2008a; Sánchez-Sánchez et al., 2018); to classify tree species (Naidoo et al., 2012); to predict forest height (Ahmed et al., 2015; Gu et al., 2018); or to relate canopy structure to burn severity patterns (Kane et al., 2014b, 2015; Mutlu et al., 2008b; García-Llamas et al., 2019). Some studies have used post-fire LiDAR data alone or as a complement to multispectral/hyperspectral imagery (Bolton et al., 2015; Kane et al., 2014b; Montealegre et al., 2014), and a few of them have employed a multitemporal LiDAR to map burn severity (McCarley et al., 2017; Wang and Glenn, 2009; White and Dietterick, 2012; Wulder et al., 2009; Stavros et al., 2016) but none of them have employed pre-fire LiDAR data to complement the information from multispectral/hyperspectral imagery in order to quantify burn severity, to our knowledge.

The maximum entropy approach (MaxEnt) (Jaynes, 1957, Phillips et al., 2004, 2006) is the algorithm we chose to implement in our study among the different automatic classifiers. It is widely used for species distribution modeling (e.g. Elith and Graham, 2009; Gill et al., 2017; Giovannini et al., 2014; Monterroso et al., 2009; Rodríguez-Veiga et al., 2016; Tittensor et al., 2009; Warren and Seifert, 2011), and it is increasingly being used in remote sensing applications: land cover change analysis (Amici et al., 2017), landslide susceptibility mapping (Felicísimo et al., 2012; Park, 2015), groundwater potential mapping (Rahmati et al., 2016); forest pest spatial distribution (Jones at al., 2015), tree species distribution (Saatchi et al., 2008) among others. There are as well many examples of using MaxEnt to model fire occurrence (Arnold et al, 2014; Chen et al., 2015a; de Angelis et al., 2015; Fonseca et al., 2016, 2017; O'Connor et al., 2017; Parisien and Moritz, 2009; Parisien et al., 2012; Peters et al., 2013; Renard et al., 2012; Tracy et al., 2018; Vilar et al., 2016). Although we did not find any burn severity studies based on MaxEnt, its characteristics encouraged us to use it in our study. This one-class classification algorithm only requires presence-only samples of a target class to be trained, thus, it constitutes an interesting alternative to other machine learning based classifiers (Li and Guo, 2010; Lin et al., 2014). In addition, it is a non-

parametric model (the input variables interrelations are not determined a priori) (Hastie et al., 2009). Furthermore, it's probabilistic output is easy to interpret and has physical meaning (Arnold et al., 2014). MaxEnt combine the presence–only samples of the target class with different variables (covariates) to calculate an estimate of probability of presence of the target class (Philips, 2017). In this way, burn severity modeling can be comparable to species distribution modeling in that multiple variables can be included in the modeling procedure (locally, topography and forest structure, regionally, climate-related factors), and known instances of each burn severity level are used to model the target distribution.

Accordingly, our study used a MaxEnt-based burn severity analysis using as input variables post-fire MESMA char fraction image from hyperspectal Hyperion data and vegetation structural variables from pre-fire LiDAR data. MaxEnt ranks the contribution of each covariate used as input and identifies the probability distribution of each burn severity level, giving the relative probability of observing the burn severity level in each pixel. Our two initial hypothesis were: 1) post-fire Hyperion data offer spectral information to characterize post-fire damage level, and 2) pre-fire LiDAR data provide spatial and structural information about pre-fire vegetation that will contribute to model and characterize each burn severity level. Thus, the principal goal of this research work is to test the effectiveness of the proposed methodology for burn severity modeling and to know the relative influence of pre-fire vegetation structure and topography on burn severity compared to the impact of post-fire damage level. Specifically, our research questions were: 1) can burn severity levels be modeled using the MaxEnt one-class classifier trained using MESMA char fraction image derived from Hyperion, and LiDAR-derived variables (canopy height, vertical vegetation distribution, terrain variables)?, 2) If yes, what are the relative contributions of the MESMA char fraction image compared to LiDAR-derived variables? Or how much compared to post-fire damage level pre-fire vegetation structure affects burn severity? 3) What are the differences in modeling each burn severity level? The approach was assessed using a large fire in central-eastern Spain.

2. MaxEnt background

A summary of MaxEnt is provided for a better understanding of the following sections. As proposed by Elith et al. (2011) we adopted a statistical point of view. More detailed information about MaxEnt can be found in Phillips et al. (2004, 2006, 2008, 2017) and Dudík and Phillips (2009). Following these authors we refer as "covariates" the independent, explanatory, or input variables; and the term "features" designates the transformations of the covariates. The software MaxEnt includes six kind of features: linear, product, quadratic, hinge, threshold and categorical. In our landscape of interest $\boldsymbol{L}$, we assume: 1) we have presence-only data, with y = 1 indicating presence, and y = 0, absence; 2) $\mathbf{z}$ denotes a vector of biophysical or environmental covariates; 3) $f(\mathbf{z})$ represents the probability density of covariates across $\boldsymbol{L}$, specifically we use $f_1(\mathbf{z})$ if the target class is present and $f_0(\mathbf{z})$ if the target class is absent; and 4) $h(\mathbf{z})$ is the vector of features.

In this context, we want to estimate the probability of presence of the target class, constrained by the environment, $\Pr(y = 1|\mathbf{z})$, with (Bayes' rule, Eq. (1)):

$$\Pr(y = 1|z) = \frac{f_1(z)\Pr(y = 1)}{f(z)} \tag{1}$$

where Pr(y = 1), is the rate of occurrence of the target class in $\boldsymbol{L}$. MaxEnt software determines the ratio $f_1(\mathbf{z})/f(\mathbf{z})$ ("raw" output), by estimating $f_1(\mathbf{z})$ in a way that it is consistent with $f(\mathbf{z})$, i.e. minimizing the distance from $f(\mathbf{z})$. Estimation of raw output is the base of MaxEnt, allowing us to know which features can be considered fundamental and which pixels are more appropriate to be included in the target class. MaxEnt defines the distance as the relative entropy of $f_1(\mathbf{z})$ with respect to $f(\mathbf{z})$. Thus, minimizing the distance (Gibbs distribution), is similar to maximizing the entropy of the raw distribution (della Pietra et al., 1997, Eq. (2)).

$$f_1(z) = f(z)e^{\eta(z)} \tag{2}$$

where $\eta(z) = \alpha + \beta h(z)$ and α ensures that $f_1(\mathbf{z})$ integrates to 1, and β, a vector of coefficients.

From Eq. (2) we can see that the MaxEnt goal is to find $\eta(\mathbf{z})$, and more precisely to find the coefficients β that satisfy the constraints without overfitting the model. To do that, MaxEnt calculates an error bound for each feature (λ_j in Eq. (3)) that includes the variation in sample values for that feature, calibrated by a tuning parameter (Eq. (3)).

$$\lambda_j = \lambda\sqrt{\frac{s^2[h_j]}{m}} \tag{3}$$

where λ_j is the regularization parameter for feature h_j, $s^2[h_j]$ the feature's variance over the m presence locations, and λ a tuning parameter. These error bounds allow L1-regularization that provides sparse solutions (Tibshirani, 1996). Regularization is a usual procedure to model selection, not being specific to MaxEnt.

In addition to raw output, the MaxEnt software (from version 3.4.0) provides by default a complementary log-log (clog-log) output, which is easier to conceptualize than raw output as it ranges between 0 and 1 and can be regarded as an estimate of probability of presence of the target class (Philips, 2017).

3. Materials

3.1. Study area

A large fire (the second largest fire in Spain in 2016, San-Miguel-Ayanz et al., 2016) burned 2291 ha in 'Carcaixent' (Valencia, central-eastern Spain) between 16 and 19 June 2016 (see Fig. 1). Nearly the entire surface had already been burned previously by large forest fires in 1981 and 1991. Thus, 78% of the surface had been burned twice before the current fire, and 10% three times or more since 1980. Only 130 ha of the 2016 fire had not been affected by previous fires (less than 5% of the total area). One of the reasons for this fire recurrence is the orientation of the Carcaixent Mountains, which trend from north-west to south-east, aligned with west winds, one of the more important factors governing the spread of fire.

The burned surface was mostly forest, mainly of Aleppo pine (*Pinus halepensis* L.), and obligate sprouting shrubs, such as kermes oak (*Quercus Coccifera* L.), chamaerops (*Chamaerops humilis* L.), lentisk (*Pistacia lentiscus* L.), heather (*Erica* spp.), strawberry tree (*Arbutus Unedo* L.), germinator rosemary (*Rosmarinus officinalis* L.), gorse (*Ulex parviflorus* L.), cade juniper (*Juniperus oxycedrus* L.) and rockrose (*Cistus* spp.). Some orange orchards can also be found in the study area (Valdecantos et al., 2016). Following the Scott and Burgan (2005) fuel models the predominant model is fuel model SH5, corresponding to stands of mature shrub lower than 2 m in height, with approximately 80% of the total area affected by the fire; followed by fuel model TU5 (understory scrub < 2 m within pine overstory), with approximately 15% of the total area, and fuel model GR4 (fine herbaceous fuel < 0.5 m, grasslands), with 5% of the total area. The study area is slightly mountainous. Most of the terrain is between 200 and 300 m (43.7%). The burned area affected a relatively flat calcareous-dolomitic massif in the upper part (high plateau) with deep ravines that open onto an agricultural plain. Slopes between 15 and 45% are dominant.

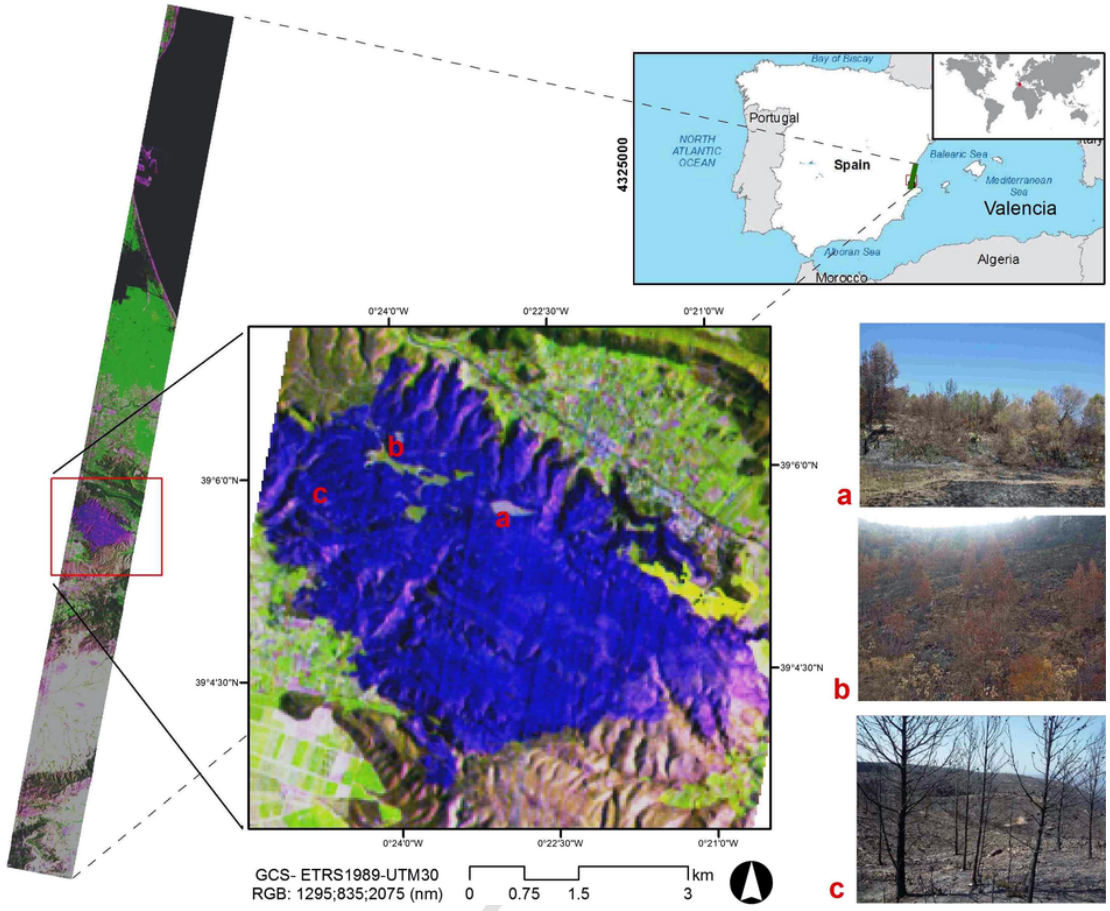

Fig. 1. Study area with photographic samples of three burn severity levels: a: low, b: moderate, c: high. EO-1 Hyperion color composition RGB: 1295:835:2075 (nm).

The annual average precipitation of the area is above 650 mm per year and average temperatures are around 17 °C (AEMET-IM, 2011). In the year previous to the fire (from 06/24/2015 to 06/24/2016), the average recorded rainfall was 364 mm, almost 50% lower than the long term average.

Burn severity is greatly influenced by fire spread. The Carcaixent Fire of 2016 started with a high intensity due to the presence of three important favorable conditions: orientation, slope and wind. This fire had a full alignment (3/3), according to the Campbell prediction system analysis criteria (Campbell, 2016). The fire began on a west facing sunken slope, with temperatures higher than 30 °C, west winds with speeds between 15 and 20 km/h and slopes between 30 and 50%. These favorable conditions caused a high severity fire. Thus the whole central strip of the burned area, corresponding to the head of the fire, was burned with high severity. Field work confirmed that the central and southern sectors of the burned area displayed a high burn severity taking into account the size of terminal branches of burned shrubs and the distribution of white ash. The burned areas with moderate burn severity corresponded mainly to the tail and/or flanks of the fire where there were losses of alignment generally with wind, slope, or both (half alignment, 2/3). Areas of moderate severity were observed in canyons at both ends of the fire perimeter. In these canyons fire had a lower intensity, probably due to the higher presence of pine and lower presence of fuel species such as strawberry tree, and better accessibility for firefighting equipment. These moderate burn severity areas were also located on the south-east part of burned area affected by the Rafelguaraf Fire in 2010, where the fire spread slower at a diminished intensity. Low severity burned areas were rare, corresponding to areas where only one of the three favorable factors of the Campbell prediction system analysis criteria were met (null alignment, 1/3). In addition to Campbell criteria, another factor must be considered when evaluating fire consequences: vegetation stress. In the Carcaixent Fire, shrub fuel moisture was low (mainly lentisk, germinator rosemary, gorse, and cade juniper enhanced propagation).

3.2. Hyperspectral data

Burn severity analysis was based on a post-fire EO-1 Hyperion scene acquired on 21st July 2016 at 8:30 UTC (sun azimuth: 95.5593 degrees, solar elevation: 40.0 degrees).

The look angle (angle from the satellite between the nadir of the satellite and the center of the targeted image) was −8.5 degrees and cloud cover between 10 and 19%. Hyperion acquires a total of 242 unique spectral channels from 357 to 2576 nm. (visible through shortwave wave infrared-SWIR-), with a spatial resolution of 30 m at nadir, though only 198 bands are calibrated in the Level 1 radiometric product. Moreover, because of an overlap between the visible and near infrared (VNIR) and SWIR focal planes, only 196 unique channels are finally present. Specifically, 8–57 for the VNIR, and 77–224 for the SWIR (EO-1 User guide, 2003). RGB: 1295:835:2075 (nm) color composition is displayed in Fig. 1.

3.3. LiDAR data

Spanish National Plan for Aerial Orthophotography (PNOA) supplied pre-fire LiDAR data. Specifically, the data were obtained in 2009 using a RIEGL sensor LMS-Q680, operating at 1064 nm with a maximum of four returns per pulse Scanner frequency and pulse repetition

were 46 Hz and 70 KHz, respectively, maximum scanning angle was 30° and mean flight height 1300 m above the level of GRS80 ellipsoid. The descriptive statistics of the total density of returns per square meter were: mean = 1.19, maximum = 1.62, minimum = 0.66, and standard deviation = 0.29. The total used points were $94{\cdot}10^6$. PNOA supplies data classified, with orthometric heights and colored with the orthophotographs captured by the PNOA.

Our study, like many others (Kane et al., 2013, 2014a; Vierling et al., 2014), does not have concurrent LiDAR and hyperspectral/multispectral data. We have a 7 year time lag between LiDAR acquisition and fire occurrence that could affect the final accuracy. The validity of LIDAR data from 2009 to represent the pre-fire vegetation in 2017 was checked by two means: 1) the official forest fire information was revised and we verified that there were no fires in this area during this period of time; and 2) we photointerpretated PNOA 2008, 2010 and 2015 orthophotographs to check whether fuel models and their spatial distribution were essentially the same. It was observed that SH5 (shrub < 2 m) was predominant in the three orthophotographs (more than 80% of the area). Thus we can confirm that 2009 LiDAR data are adequate for representing pre-fire vegetation.

3.4. Additional data

The official burn severity map produced by the regional government (FFPS, 2016) was used to define the presence-only samples for training the MaxEnt classifier to model each burn severity level. Additionally, it was also used to digitize polygons over the orthophotograph from which candidate char endmember spectra were obtained. This official map was calculated from Sentinel-2 MultiSpectral Instrument (MSI) data, and employed three burn severity levels: low, moderate and high. Specifically, 10/06/2016 and 20/06/2016 images were used as pre- and post-fire data to calculate the Relative delta Normalized Burn Ratio (RdNBR, Miller and Thode, 2007). RdNBR was classified by using the methodology proposed by Botella-Martínez and Fernández-Manso (2017) what allowed to obtain a burn severity map. This method uses as field reference the aerial photographs of the Security and Emergency Response Agency of the Autonomous Government of Valencia that were taken from helicopters during and after the large fire. From the aerial photographs sample plots of approximately 30x30m are defined and their burn severity level is visually identified by adapting the procedure proposed by Parsons et al., (2010). Classification accuracy was assessed by field measurements and was higher than 80% (see FFPS, 2016 for more details).

Additionally, the Spanish National Center of Geographic Information (CNIG) through the PNOA agency supplied a 0.25 m-pixel digital orthophotograph recorded in 2015 that helped to determine the candidate endmember spectra for the MESMA procedure.

A 5 m Digital Elevation Model (DEM) supplied also by the Spanish PNOA was employed to derive the topographic variables (aspect and slope) used as covariates in MaxEnt.

Finally, a pre-fire Landsat 8 Operational Land Imager (OLI) scene recorded on 9 June 2016 (ten days before the fire) enabled us to characterize pre-fire vegetation greenness and compare its influence on burn severity to the influence of pre-fire vegetation structure (based on pre-fire LiDAR data).

4. Methods

4.1. Processing of hyperspectral EO-1 Hyperion data

The EO-1 Hyperion image was supplied at a processing level 1T (L1T), that includes VNIR-SWIR alignment, radiometric and systematic geometric corrections based on a 90 m DEM and ground control points, and georeferencing to the coordinate system UTM-WGS84-30 N. All of the bands were individually displayed and those bands that showed bad lines, striping or very high noise were discarded (George et al., 2014). We finally kept 106 bands from 426 to 2395 nm. Subsequently, we co-registered the Hyperion data to the orthophoto provided by the PNOA agency using a first order polynomial and nearest neighbor resampling. The maximum mis-registration error was 0.25 of a pixel. We then corrected the data atmospherically and transformed them to surface reflectance using the FLAASH algorithm in ENVI that incorporates the MODTRAN radiation transfer code (Berk et al., 1989; Mathew et al., 2000). In our study, the main input parameters of the FLAASH model for the Hyperion image were: atmospheric model: mid-latitude summer (water vapor: 3636 std atm-cm, surface air temperature: 21 °C, and water vapor: 2.92 g/cm^2); aerosol model: rural; and water retrieval: Hyperion bands covering the 1135-nm water vapor band were used. Finally, Visualization and Image processing for Environmental Research (VIPER) tools software (Roberts et al., 2007) was used to unmix the surface reflectance. This software operates as an add-on for the ENVI software package and was generated at the Department of Geography at University of California Santa Barbara.

The MESMA procedure consisted of three stages: 1) defining candidate endmembers to create a spectral library; 2) selecting the more adequate endmembers to build the definitive spectral library; and 3) unmixing each pixel to calculate the fraction images. A spectral library that incorporates endmember spectra representing the different land cover or material types present in a scene is the base of MESMA procedure (Roberts et al., 1998). Thus, this algorithm enables that a different set of endmember spectra (model) unmixes each pixel. The model that minimizes the RMSE and fulfills all constraints is finally chosen to unmix the pixel (Roberts et al., 1998). Selection of the appropriate endmembers is an indispensable factor for a successful unmixing approach (Tompkins et al., 1997). VIPER tools 1.5 includes three options to help in the choice of the most adequate endmembers to build the definitive spectral library: 1) Countbased Endmember Selection (CoB, (Roberts et al., 2003); 2) Endmember Average RMSE (EAR, Dennison and Roberts, 2003); and 3) Minimum Average Spectral Angle (MASA, Dennison et al., 2004).

As previous works did (see Dudley et al., 2015; Roberts et al., 2015) selection of candidate endmembers was based on high spatial resolution ortophotographs where we defined georeferenced uniform polygons comprising only one class. Next, to build the definitive spectral library, CoB, EAR and MASA were employed. CoB allowed us to select the endmembers that model the maximum quantity of endmembers within their class; EAR, the endmembers that produced the minimum RMSE within a class; and MASA, the endmembers that showed the minimum average spectral angle. As suggested by Roberts et al. (2007), we also considered our knowledge of the study area and the typical shape of the spectra in the endmember selection process.

Once a definitive spectral library was built, in accordance with Quintano et al. (2017), we arranged the endmembers forming three spectral libraries: non-photosynthetic vegetation and soil (NPVS), green vegetation (GV), and char. We used similar constraints for maximum/minimum admissible fraction values (0.10/−0.10), maximum value of shade fraction (0.85), maximum acceptable RMSE (0.025), and minimum number of classified pixels (90% of the image) as previous MESMA research works (Dudley et al., 2015; Quintano et al., 2013, 2017). If the number of classified pixels requirement was not satisfied, the type and/or number of spectra included in the definitive spectral libraries were modified and the hyperspectral image was unmixed again. Once the definitive MESMA fraction images were obtained they were shade normalized. Shade normalization implies removing the shade endmember, and thus incorporating novel information about the relative abundance of nonshade endmembers.

4.2. Processsing of LiDAR data

Discrete return LiDAR data from PNOA was already coregistered to the PNOA orthophotographs, so we did not need to perform this pre-processing. The rest of LiDAR processing operations were carried out using FUSION software package (http://forsys.cfr.washington.edu/fusion/fusionlatest.html; McGaughey, 2018) from US Forest Service. First, laser pulses were grouped into vegetation points and ground pulses, and a 10 m DEM was calculated from the ground pulses (García-Llamas et al., 2019). Next, height of pre-fire vegetation was computed by subtracting the DEM from the z-values of laser pulse returns. We did not take into consideration height values lower than 0.5 m to avoid multiple backscattering returns and small local depressions. This decision was based on previous studies that recommended discarding this kind of potentially erroneous laser returns (e.g. Erdody and Moskal, 2010; Estornell et al., 2011; Marino et al., 2016;). Height values higher than 20 m were also discarded to avoid undesired returns from power lines, assuming that 20 m is the maximum height of vegetation.

We determined a 30 × 30 m grid to match the resolution of Hyperion. Vertical structure of pre-fire vegetation was defined by classifying the vegetation height profile into percentiles based on their height distribution within the 30 × 30 grid. Moreover, means, maximums, and coefficients of variation of vegetation return heights within the grid were also taken into account. Regarding the horizontal structure (canopy closure), three parameters were taken into consideration to be included as input to the MaxEnt one-class classifier: canopy cover (CC), canopy relief ratio (CRR) and canopy ratio (CR). CC was calculated as the ratio between the number of all returns above 0.5 m and the total number of first returns. CRR (Pike and Wilson, 1971; Parker and Russ, 2004) measures the relative shape of the canopy from mean, minimum, and maximum canopy heights. Finally, CR (Smith, 1986), related to tree vigor, is the ratio of canopy height depth (20th percentile height of vegetation points) to total tree height (90th percentile height of vegetation points). All the calculated LiDAR-derived metrics were identified in previous studies as highly correlated with vegetation structure and/or fuel load (Cao et al. 2019; Erdody and Moskal, 2010; Kane et al., 2015; Naidoo et al., 2012; Marino et al., 2016, 2018).

4.3. Processing of Landsat 8 OLI data

The USGS Landsat 8 surface reflectance product acquired on 6 June 2016 was downloaded to compute two spectral indices related to pre-fire vegetation greenness: Normalized Difference Vegetation Index (NDVI) and Normalized Difference Water Index (NDWI). NDVI is sensitive to vegetation chlorophyll content and has been widely used to quantify the net primary production of vegetation (e.g. Ricotta et al., 1999). NDWI is related to vegetation water content (Gao, 1996) and vegetation architectural parameters (Anderson et al., 2010). Both of them have proven to show a strong relationship to live fuel moisture (Dennison et al., 2005). They were included as covariates for MaxEnt procedure instead of LiDAR-derived variables (see Table 1) to compare the influence of pre-fire vegetation greenness on burn severity to the influence of pre-fire vegetation structure (based on pre-fire LiDAR data).

4.4. MaxEnt classification

Our study was based on the MaxEnt software (version 3.4.1) developed by Phillips et al. (2004, 2006), and updated by Phillips et al. (2017). MaxEnt needs two types of input data exclusively: presence-only training samples and some predictive-continuous variables or co-variates of the complete study area. The presence-only data were obtained by randomly sampling each target class or burn severity level from the official burn severity map used as ground reference. From these presence-only inputs the MaxEnt software knows the burn severity level and the coordinates of each input sample that will be related to the different covariates. In our study, we compared the impact of two pre-fire vegetation characteristics on burn severity: pre-fire vegetation structure and pre-fire vegetation greenness. LiDAR-derived variables provided both vertical and horizontal structural information about pre-fire vegetation. Vegetation greenness was represented by NDVI and NDWI computed from pre-fire Landsat 8 OLI image. Post-fire MESMA char_sn give information about post-fire vegetation damage to the modeling algorithm. As topographic variables, we included slope and aspect obtained from the 5 m PNOA DEM after aggregating it to a 30 m grid. Table 1 shows the employed covariates in both cases that MaxEnt procedure was employed (LiDAR- and DEM derived covariates in the first case, and Landsat- and DEM-derived covariates in the second case).

Table 1
Summary of the covariates used by MaxEnt.

Post-fire vegetation damage (EO-1 Hyperion-derived metrics)	
Description	*Acronym*
MESMA char fraction image shade normalized	Char_sn
Vertical structure of pre-fire vegetation (LiDAR-derived metrics)	
Description	*Acronym*
Maximum height of the vegetation points (m)	EM
Mean height of all vegetation points (m)	Em
Coefficient of variation of the vegetation points (m)	ECV
10th percentile height of the vegetation points (m)	EP10
20th percentile height of the vegetation points (m)	EP20
50th percentile height of the vegetation points (m)	EP50
90th percentile height of the vegetation points (m)	EP90
Horizontal structure of pre-fire vegetation (LiDAR-derived metrics)	
Description	*Acronym*
Canopy Cover (%)	CC
Canopy relief ratio	CRR
Canopy ratio (%)	CR
Topographic variables (DEM-derived metrics)	
Description	*Acronym*
Slope (degrees)	SL
Aspect (degrees)	AS
Elevation (m)	DEM
Greenness of pre-fire vegetation (Landsat 8 OLI derived variables)	
Description	*Acronym*
Normalized Difference Vegetation Index	NDVI
Normalized Difference Water Index	NDWI

We allowed MaxEnt to automatically establish the optimal complexity level from the sample size of presence-only data (default option) as previous studies did (e.g. Li and Guo, 2010; Radosavljevic and Anderson, 2014). In our study, we trained MaxEnt with 140 of low burn severity, 126 of moderate burn severity and 137 samples of high burn severity. As we used a relatively high number of presence-only samples, the program was not limited to employing simple features and could perform modeling with all the complexity required.

The random test percentage was set to 25% as in previous studies (Chen et al., 2015a; Arpaci et al., 2014; Vilar et al., 2016) so 75% of the samples were employed for MaxEnt training. We used the default values for the rest of user-specified parameters accordingly to different works that stated they performed well (Dudík et al., 2004; Phillips and Dudík, 2008): number of background samples = 10000, regularization multiplier = 1, maximum iterations = 500, and convergence threshold = 10^{-5}. MaxEnt allows for replication, which generates

more reliable results. We used 10 replicates with repeated subsampling scheme.

MaxEnt includes receiver operating characteristic (ROC) analysis for model assessment. In a ROC analysis, area under the curve (AUC) (Bradley, 1997) represents the model's capacity to predict correctly presence (sensitivity) and absence (specificity). It is currently considered an established procedure to evaluate the accuracy of predictive distributions (Fawcett, 2006). AUC values range between 0 and 1 as it can be regarded as a part of area of the unit square. Moreover, an AUC value equal to 0.5 represents a random prediction of presence and absence (diagonal line). AUC values ranging from 0.5 to 0.7 indicate poor model performance, from 0.7 to 0.9 indicate a moderately good performance, and from 0.9 to 1 indicate excellent model performance (Swets, 1988).

5. Results

Table 2 summarizes the endmember selection process, displaying the endmember categories included in each definitive spectral library. The GV spectral library was defined from endmember spectra grouped into three categories: forest, maquis shrubland and grassland. The CHAR spectral library was built from endmembers located inside the fire perimeter. NPV and soil formed one spectral library, NPVS, as in a previous related study (Quintano et al., 2017). The NPVS spectral library included NPV, roads and urban areas (Impervious surfaces) and limestone (pervious surface). Once the definitive spectral libraries were defined (based on CoB, MASA and EAR, the spectral shape of the spectra and our knowledge of the study area), unmixing of Hyperion data was performed until the number of classified pixels was acceptable by varying the type and/or number of spectra contained in each spectral library. We unmixed the hyperspectral image by using 4 endmember models although it was also possible to use 2 or 3 endmember models. Fig. 2 (right) shows examples of the selected endmember spectra from each spectral library. In our study, the percentage of unclassified pixel inside the fire perimeter was finally 0.09%, and 224 models were employed (see Table 2).

Table 2
MESMA definitive spectral libraries with their endmember spectra, and summary of unmixing results.

Level 1	Level 2	Level 3	Spectral library
Green vegetation	Forest	Alleppo pine	Green vegetation (GV)
		Orange trees	
	Maquis shrubland	Kermes oak	
		Lentisk	
	Grassland	Golf courses	
Char		High burn severity	CHAR
		Moderate burn severity	
Soil	Pervious	Limestone	Non-photosynthetic vegetation and soil (NPVS)
	Impervious	Roads	
		Urban areas	
No photosynthetic vegetation		Non irrigated lands	
Unmixing results	# Endmembers in NPVS		4
	# Endmembers in GV		7
	# Endmembers in CHAR		8
	# Models used in unmixing		224
	Image unclassified inside fire perimeter (%)		0.09

We shade normalized the definitive MESMA fraction images. Fig. 2 (left) shows the visual discrimination between unburned and burned areas in both shade normalized char fraction (char_sn) and shade-normalized GV fraction (GV_sn). We distinguish level differences in the burned area that we assume can be associated with burn severity. In the shade-normalized NPVS fraction (NPVS_sn) some agricultural patterns and roads are evident in the left-lower corner but the interpretation of NPVS_sn fraction in the burned area is more complicated. Thus, the visual analysis indicates that there is relation between burn severity and char_sn and GV_sn MESMA fraction images.

Once the set of covariates from Hyperion, LiDAR, Landsat and the DEM were ready (see Table 1), MaxEnt modeled each of the three burn severity levels twice. The first time Hyperion-, LiDAR- and DEM-derived covariates were used; the second time we used as covariates Hyperion-, Landsat and DEM-derived metrics. A summary of the main MaxEnt parameters in both cases is displayed in Table 3. To assist us in the selection of the best model among the 10 replicates, we used the maximum test AUC value as recommended by Warren and Seifert (2011), who affirmed that this measure is not affected by overfitting as overfitting the model does not necessarily increase the match to independent test data. The average model represents the model obtained by averaging the parameters achieved in each of the 10 replicates.

MaxEnt defines gain as the average log probability of the presence samples, minus a constant to force the uniform distribution to have zero gain (Philips, 2017). This gain shows how closely the model is concentrated around the presence samples. Thus, a gain of 1.1493 (first case, high burn severity, best model) indicates that the average likelihood of the presence samples is exp(1.1493) $\approx$ 3.2 times higher than that of a random background pixel. Table 3 shows both regularized and unregularized gains. We noticed that for high and moderate burn severity levels, the values are quite similar but low burn severity level displays lower gain values in both cases. Regarding the AUC test, we observed approximately similar AUC test values for high and moderate burn severity (always higher than 0.8) and slightly lower ones for low burn severity. Indeed, AUC test values are slightly higher when LiDAR derived variables were used. Specifically, when considering the best models AUC test values were 0.85 for high burn severity level, 0.88 for moderate and 0.81 for low, indicating a good performance of the model, especially for the moderate level, which can be considered as having excellent performance (Swets, 1988). The training AUC values showed the same trend, although they were higher than the AUC test values (always > 0.85, and higher than 0.88 for high and moderate burn severity levels in the first case). An increasing tendency for the AUC standard deviation in the first case was observed from high to low burn severity levels, showing again that the model for high and moderate levels performed better. In the second case, we have higher values than in the first one, suggesting a poorer performance of the second MaxEnt process (using Landsat-derived spectral indices). Knowing how each covariate contributes to the final model is important (Baldwin, 2009). MaxEnt provides the gain of the model with each feature included during the training process, transformed to percentages, which provides a convenient method for comparison. Thus, Table 3 also shows the percentage of contribution of the different types of covariates used in each case. In both cases the contribution of post-fire vegetation damage (via char_sn image from hyperspectral data) was the most relevant, and the other covariates complemented its information.

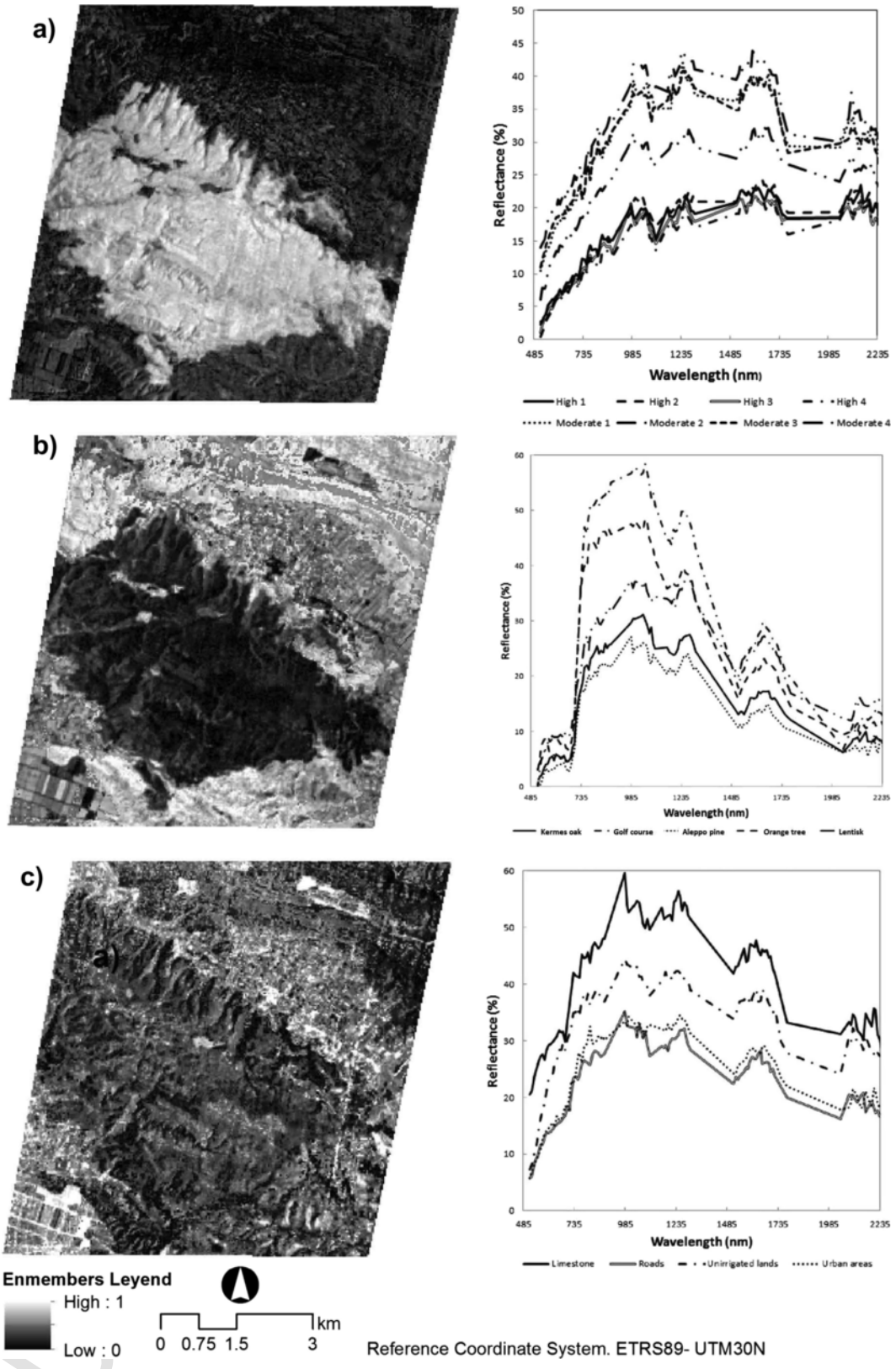

Fig. 2. Left: Shade normalized EO-1 Hyperion MESMA fraction images. a) shade normalized char fraction (char_sn); b) shade normalized green vegetation fraction (GV_sn); c) shade normalized non-photosynthetic vegetation and soil fraction (NPVS_sn); Right: Example spectra. a) char spectral library; b) green vegetation (GV) spectral library; c) non-photosynthetic vegetation and soil (NPVS) spectral library.

This fact was particularly true for the MaxEnt process that used Landsat data where the percentage of contribution of char_sn was higher than 88% for all three burn severity levels (considering both the best and the average model). The total contribution of both Landsat-based spectral indices was relatively low and similar to the total contribution of LiDAR-derived metrics related to pre-fire structure (approximately 8%).

Table 3
Summary of parameters of MaxEnt modeling processes.

1.-Covariates: Hyperion-, LiDAR- and DEM-derived metrics						
	High burn severity		Moderate burn severity		Low burn severity	
	Best model	*Average model*	*Best model*	*Average model*	*Best model*	*Average model*
Regularized training gain	0.9862	1.0107	0.9536	1.0179	0.6882	0.7174
Unregularized training gain	1.1493	1.1656	1.1573	1.2062	0.902	0.9332
Training AUC	0.8830	0.8826	0.8872	0.8918	0.8527	0.8532
Test gain	0.9484	0.8143	1.0700	0.8060	0.6590	0.5130
Test AUC	**0.8481**	**0.8327**	**0.8761**	**0.8392**	**0.8145**	**0.7856**
AUC Standard Deviation	0.0146	0.0171	0.0157	0.0214	0.0272	0.0304
#Training samples	137	137	126	126	140	140
#Test samples	45	45	42	42	46	46
PC post-fire char_sn	73.86	74.95	70.42	72.73	54.45	54.27
PC pre-fire veg. structure	7.44	9.40	11.65	9.40	24.82	28.52
2.-Covariates: Hyperion-, Landsat- and DEM-derived metrics						
	High burn severity		**Moderate burn severity**		**Low burn severity**	
	Best model	*Average model*	*Best model*	*Average model*	*Best model*	*Average model*
Regularized training gain	0.9732	1.0237	0.9418	1.0154	0.8134	0.8334
Unregularized training gain	1.1723	1.2023	1.1773	1.2205	0.9123	0.9451
Training AUC	0.8827	0.8733	0.8723	0.8603	0.8613	0.8514
Test gain	0.9373	0.8444	1.0834	0.9035	0.8733	0.7924
Test AUC	**0.8473**	**0.8227**	**0.8631**	**0.8245**	**0.8233**	**0.7843**
AUC Standard Deviation	0.0157	0.1832	0.0167	0.2481	0.0283	0.0321
#Training samples	137	137	126	126	140	140
#Test samples	45	45	42	42	46	46
PC post-fire char_sn	87.12	88.21	88.13	90.62	87.14	88.53
PC pre-fire veg. greenness	8.40	8.12	5.31	4.82	4.71	4.14

Note: Best model: model with the maximum test AUC; Average model: average model of the 10 replicates, average values are provided by MaxEnt, PC: percentage of contribution; veg.: vegetation.

Regarding the moderate burn severity level, the total contribution of pre-fire vegetation structure increased till 10–11%. Conversely the total contribution of pre-fire vegetation greenness decreased to approximately 5%. This trend was observed as well for the low severity level, in which the total contribution of pre-fire vegetation structure was approximately 25%, whereas the total contribution of pre-fire vegetation greenness added approximately 5%. Considering the low percentage of contribution of pre-fire vegetation greenness, particularly when it was compared to the percentage of contribution of pre-fire vegetation structure we chose the MaxEnt process that includes LiDAR-derived metrics as covariates to obtain the suability surface of each burn severity level.

Fig. 3 displays the ROC curves of the MaxEnt process using LiDAR-derived covariates (best model and averaged over the 10 replicate runs). The curves corroborate the above statements. Finally, from Table 3 and Fig. 3 we can answer our first research question, and confirm that burn severity may be modeled using the MaxEnt one-class classifier trained using MESMA fraction images derived from Hyperion data, LiDAR-derived variables (canopy height, vertical vegetation distribution, terrain variables) and topographic variables derived from a DEM.

Table 4 shows the percentage of contribution of each covariate to the final model. From it several facts can be highlighted. First, covariates from the Hyperion data displayed the most important contribution to the final model; although their contribution decreased from the high to low burn severity level. Regarding the set of LiDAR-derived metrics ECV followed by EP10 had the highest contribution to the high burn severity model, EP10 folowed by Em and EP90 to the moderate burn severity and EP10 followed by ECV, EP90 and EM, to the low burn severity level. Summarizing, we can confirm that EP10, ECV and EP90 were the most relevant structural metrics in the three levels. The global contribution of this group of variables is similar for high and moderate burn severity (approximately 5%) although the contribution to the low burn severity level is more important (16.27%–19.95%). With respect to the group of LiDAR-derived metrics related to the horizontal structure of pre-fire vegetation, they increased their total contribution from high to low burn severity (1.90%–3.93% in high vs 8.58.55%–8.57% in low burn severity). In general terms, CC was the metric with highest contribution and CRR the metric with the lowest one. Thus, the final contribution of all LiDAR-derived metrics (representing both vertical and horizontal structure of pre-fire vegetation) shows an increasing trend from high to low burn severity level (7.44%–9.36% for high and 24.83%–28.52% for low). Finally, concerning the topographic variables, AS and DEM showed the highest contribution (DEM to the high burn severity level, and AS to the moderate and low). The percentage of contribution to the final model of all DEM-derived covariates is approximately similar for the three burn severity levels (approximately 20% for the best model and slight lower for the average model).

From the Jackknife diagrams for the regularized training gain and test gain (Fig. 4), we can also observe which covariates are most important in the model. Concerning the low burn severity level (greenish lines on Fig. 4) the contribution of all covariates is quite similar regarding the training and test gain. No important differences are observed between both Jackknife diagrams. The char fraction image showed the highest contribution in both of them, indicating that it helped MaxEnt to fit the model to the training data and also to make the model transferable. AS was the second covariate in importance to the test gain both when it was excluded ('without' on Fig. 4) and when it was considered in isolation ('with' on Fig. 4), and the second as well to the training gain (option 'without'). Following AS, we could mention CC, EP50 and EP90.

With regards the moderate burn severity level (bluish lines on Fig. 4) again no substantial differences were observed between the training and test gain Jackknife diagrams. The char fraction showed the highest contribution in all cases, followed by AS (option 'without") and CC for the test gain. Basically the same covariates contributed to low and moderate burn severity levels. The char fraction again was the covariate that most contributed to the high burn severity level, followed, in this case, by DEM both in train and test gain ('without' and 'with' options). The jackknife diagrams were performed for the 10 replicates and showed similar patterns with slight variability in gain values. Information from Fig. 4 basically agrees with the information shown in Table 4: Hyperion char fraction had the highest contribution in all burn severity levels; DEM was the second contributor to the high burn severity class, and AS to moderate and low burn severity levels; CC and EP10 were the third and fourth contributors, in particular, to moderate and low burn severity levels.

Table 4 and Fig. 4 allow us to answer the last two initial research questions. Hyperspectral data (MESMA fraction image) have an important contribution to the final model of burn severity ranging from more than 50% for low burn severity level to approximately 75% for high

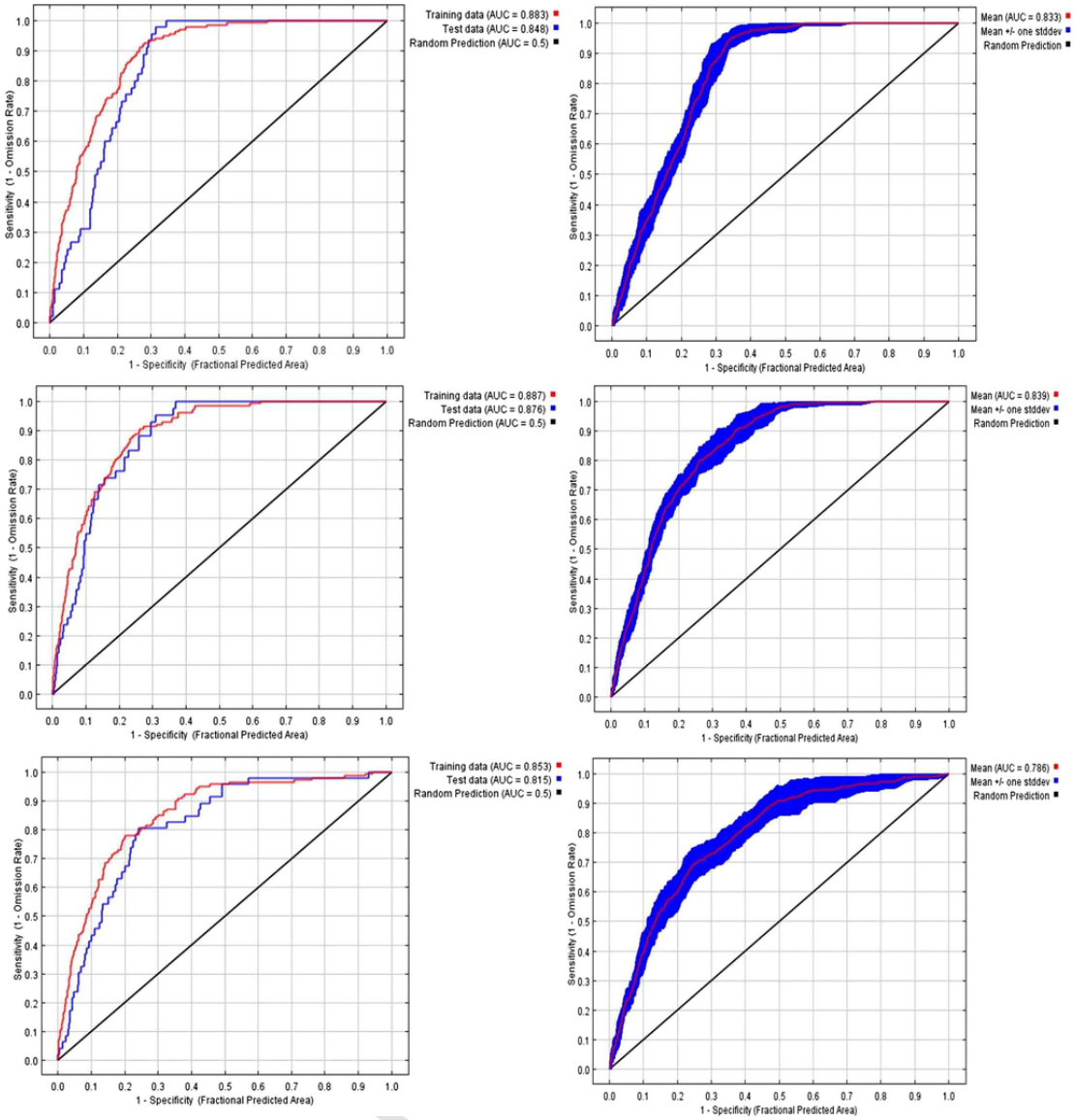

Fig. 3. ROC curves. Left: best model, right: averaged over the 10 replicate runs; higher: high burn severity level, middle: moderate burn severity level; lower: low burn severity level.

burn severity level. The contribution of the LiDAR data though lower was also important; it reached approximately 25% for low burn severity level. Its contribution was lower for the high burn severity level, around 8%. It can be observed that each burn severity level displays a different pattern.

Finally, Fig. 5 shows the estimate of the probability of presence of a specific burn severity level for the best model (maximum test AUC) that can be seen as the suitability surface for each burn severity, particularly, Fig. 5a) for low burn severity level, Fig. 5b), for moderate, and Fig. 5c) for high). Fig. 5d) displays a color composition of the suitability surfaces of the three burn severity levels (shown in Fig. 5a) 5b) and 5c). The most suitable surface for high burn severity corresponds to the whole study area excluding borders, and some interior valleys, which agrees with observed severities. Moderate and low burn severity levels were confined to the borders of the fire and to some valleys which agrees with the suitability surface displayed respectively in Fig. 5b) and 5c).

6. Discussion

The high number of pixels classified by the MESMA procedure (constrained to the error limits reflected on the Methods section) suggests that a satisfactory endmember selection process was carried out. Though we employed four categories for describing the variability of the Hyperion data: green vegetation, non-photosynthetic vegetation, soil and char, they were combined into three spectral libraries: GV, NPVS and char. As Quintano et al. (2017) suggested including NPV and soil in a unique spectral library provides accurate results when the class of interest is burned area. Moreover, the present work, corroborates the suitability of CoB (Roberts et al., 2003), EAR (Dennison and Roberts, 2003), and MASA (Dennison et al., 2004) to guide a successful selection of the definitive endmember spectra from the candidate spectral library as many previous works did (Fernández-Manso et al. 2012; Franke et al., 2009; Lippitt et al., 2017; Quintano et al., 2013; Roberts et al., 2012; Youngentob et al., 2011).

In our study, MESMA shade normalized char fraction image showed the most important contribution to the final model of burn severity (see Table 4). The relationship between char fraction and burn severity has

Table 4
Percentage of contribution of each covariate.

Pot-fire vegetation damage (EO-1 Hyperion-derived metrics)						
Covariates	*Best model*			*Average model*		
	High	*Mod.*	*Low*	*High*	*Mod.*	*Low*
Char_sn	**73.86**	**70.42**	**54.45**	**74.95**	**72.73**	**54.27**
Vertical structure of pre-fire vegetation (LiDAR-derived metrics)						
Covariates	*Best model*			*Average model*		
	High	*Mod.*	*Low*	*High*	*Mod.*	*Low*
EM	0.27	0.00	2.65	0.06	0.06	4.48
Em	0.05	1.62	0.02	0.01	0.69	1.85
ECV	**3.31**	0.16	2.81	**3.29**	0.61	2.96
EP10	1.45	**2.57**	**5.52**	0.97	**1.86**	**5.85**
EP20	0.39	0.01	2.04	0.52	0.16	0.21
EP50	0.00	0.06	0.55	0.20	0.35	0.51
EP90	0.06	0.76	2.69	0.41	0.69	4.10
Total	**5.53**	**5.18**	**16.27**	**5.47**	**4.42**	**19.95**
Horizontal structure of pre-fire vegetation (LiDAR-derived metrics)						
Covariates	*Best model*			*Average model*		
	High	*Mod.*	*Low*	*High*	*Mod.*	*Low*
CC	**0.84**	**4.70**	**4.55**	**2.83**	**3,26**	**4.00**
CRR	0.40	0.80	1.61	0.45	0.66	1.68
CR	0.66	0.96	2.39	0.65	1.05	2.89
Total	**1.91**	**6.47**	**8.55**	**3.93**	**4.98**	**8.57**
Topographic variables (DEM-derived metrics)						
Covariates	*Best model*			*Average model*		
	High	*Mod.*	*Low*	*High*	*Mod.*	*Low*
SL	1.36	2.33	1.04	1.63	4,56	2.24
AS	6.19	**13.02**	**12.81**	3.86	**11.25**	**12.52**
DEM	**11.15**	2.59	6.84	**10.17**	2,05	2.45
Total	**18.70**	**17.94**	**20.68**	**15.66**	**17,86**	**17.21**

already been pointed out by previous studies. Fernández-Manso et al. (2009), Hudak et al. (2007), Lentile et al. (2009), and Sunderman and Weisberg (2011) confirmed it with a char fraction obtained by using SMA; whereas that Quintano et al. (2017), Tane et al. (2018), Veraverbeke and Hook (2013), and Veraverbeke et al. (2014) employed MESMA to calculate the char fraction. Most of previous studies used multispectral Landsat data, however, Tane et al. (2018) and Veraverbeke et al. (2014) unmixed hyperspectal AVIRIS data.

Although the MaxEnt model relied mostly on the MESMA fraction images for modeling of the suitable surface of the different burn severity levels, LiDAR-derived metrics had an important contribution (approximately 25% for the low burn severity level). LiDAR data has been shown also to be a lesser contributor to species discrimination (Alonzo et al., 2013, 2014), although Kane et al. (2015) and Wulder et al. (2009) did not find LiDAR-derived forest structure as a key driver of burn severity. In our study, among the variables that define vertical structure of pre-fire vegetation, EP10 had a relatively important contribution in the three burn severity levels and CC displayed the maximum contribution among the LiDAR-derived metrics related to horizontal structure. The relationship between LiDAR derived variables and burn severity has already been shown by previous research works. Montealegre et al. (2014) observed that LiDAR-derived height variables showed the strongest correlation with burn severity, followed by variables related to percentage of returns above a height threshold (as CC in our study). García-Llamas et al. (2019) applied random forest to assess the effect of several environmental factors on burn severity and identified ECV as a LiDAR-derived metric present in the final model. The study area of both of these studies was a tree-forested area, where vertical structure was a determining factor. Our study area, however, is dominated by shrubs (with a uniform and relatively low vertical structure). Thus, horizontal structure parameters had more importance than vertical ones to characterize the pre-fire vegetation. Hopefully, as summarized by Vogeler et al. (2016) the availability (temporal and spatial) of LiDAR data will increase in the future. Thus, we could combine them with multi/hyperspectral imagery to improve burn severity mapping, among other applications.

Our results show that the influence of pre-fire vegetation structure on the low burn severity class was higher than the high severity level, contrary to what might appear at first sight. We suggest two possible explanations. First, the information supplied by the char fraction image modeled the high burn severity level with such high performance that there was no room for any contribution from other covariates. Conversely, char fraction image was not as a good a predictor of moderate and particularly low burn severity level allowing other covariates to contribute to improved models of burn severity. Previous burn severity studies based on char fraction image have also modeled the high burn severity level with higher accuracy or have identified some confusion between moderate and low classes (Quintano et al., 2013; 2017). Second, our results only pointed out the influence of pre-fire vegetation structure on burn severity but they did not give any information about whether their relationship is positive or negative. Thus, they do not disagree with previous studies showing that higher complexity of vegetation structure produces high burn severity (Baker, 2014; García-Llamas et al., 2019). Simply, in our study the pre-fire vegetation structural information provided by LiDAR-derived metrics helped to model the moderate and low burn severity levels in a greater extend than the high severity level.

With regard to the contribution of Landsat-derived covariates, we observed a lower contribution of the Landsat-derived spectral indexes representing pre-fire vegetation greenness than the LiDAR-derived metrics representing pre-fire vegetation structure. Our results suggest that pre-fire vegetation structure had a higher influence on burn severity than pre-fire vegetation greenness in this large fire. Conversely, in a mega-fire in a forest of transition between Mediterranean and Atlantic climate García-Llamas et al. (2019) found that fuel load had a higher impact on burn severity than vegetation structure. Both studies, however, suggest that burn severity does not depend only on the existence of dense live biomass accumulations, but also on the vertical structural arrangement of those fuels. Although the availability of dense biomass may define fire sustainment, vertical structural complexity determines the vertical fire propagation (Agee and Skinner, 2005). Pine forests are frequently affected by high severity crown fires due to the stratified pattern of pine crowns and to the fuel vertical structure that intensifies vertical fire spread (Broncano and Retana, 2004; Fernandes and Rigolot, 2007). In our study area, vertical structure depends on: 1) a relative tall (up to 2 m) understory including different shrubs as kermes oak, lentisk or strawberry tree, and 2) a stock of ladder fuels (especially low branches of the trees).

Finally, regarding the DEM-derived variables, their total contribution to the final model was approximately the same for the three burn severity levels (around 20%). Assuming fire hierarchy (Heyerdahl et al., 2001), fire is affected by the so-called top-down and bottom-up controls. As Kane et al. (2015) summarized top-down controls (mainly variations in precipitation and temperature) determine fire uniformity over large areas, whereas bottom-up controls (mainly topography) result in microclimate and local vegetation structure that have impact on fuel loading, moisture, and fire behavior. Hoden et al. (2009) corroborated that the important relation between burn severity and topography indicates the importance of bottom up vegetation and topographic controls to burn severity. Many other studies have also pointed out this relationship. Tracy et al. (2018) highlighted the contribution of slope for the three burn severity levels. In their study, where 90 vari-

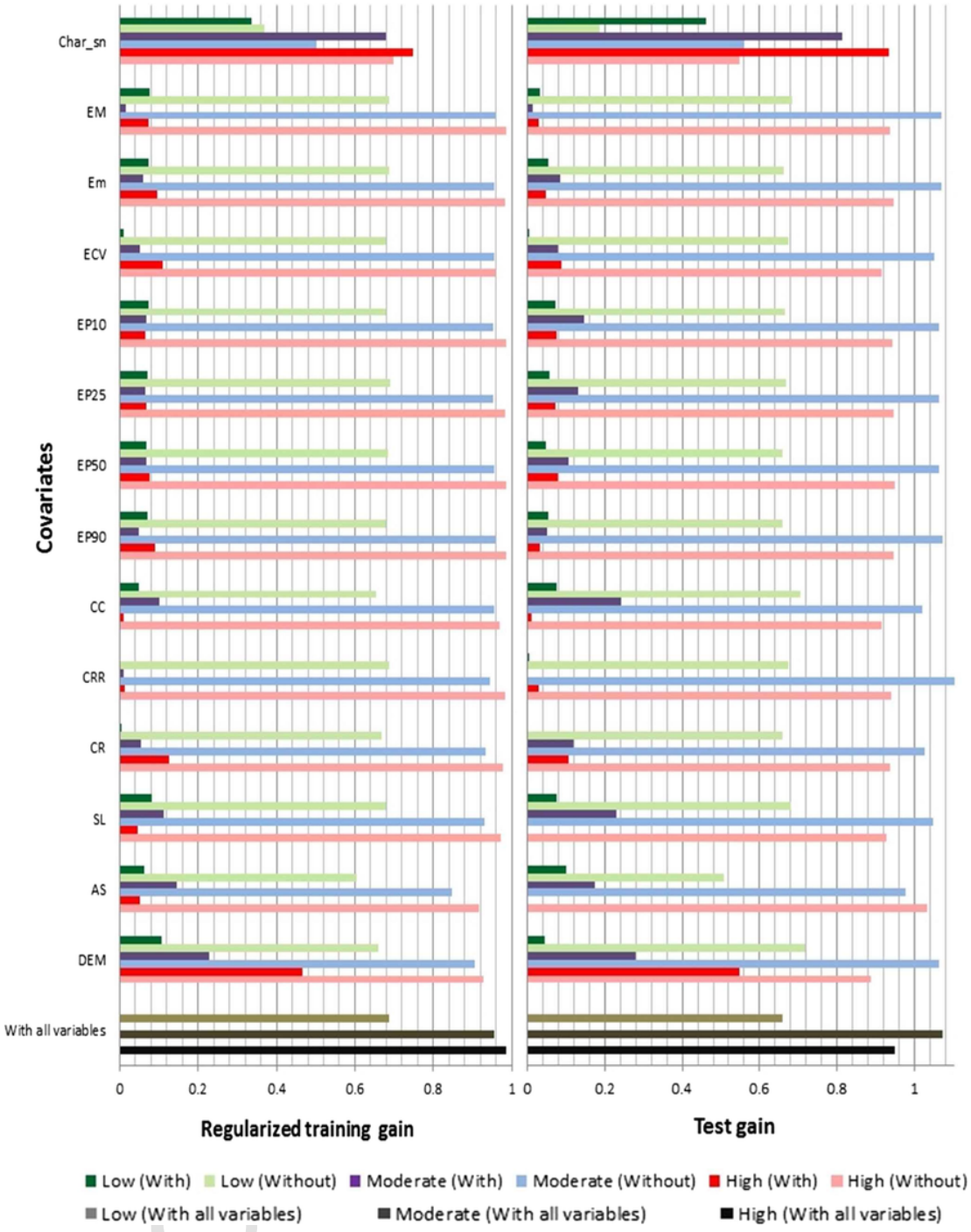

Fig. 4. Jackknife diagrams of the best model of the 10 replicates (maximum test AUC) for regularizaed training gain and test gain. MaxEnt software provides these parameters excluding the covariate of interest ('without' on Figure); only with the variable of interest ('with' on Figure) and "with all variables".

ables were tested in relation to their influence on wildfire activity, slope appeared among the top ten ranked variables. Analyzing the Rim Fire (2013, Yosemite National Park, USA), Harris and Taylor (2015) and Lydersen et al. (2014) concluded that elevation was a strong predictor of burn severity. Similarly Estes et al. (2017) found that slope position and aspect were the topographic variables that most influenced burn severity in Klamath Mountains fires (California, USA) of 2006. As they summarized, elevation is related to the changes in temperature following the adiabatic lapse rate; aspect determines the solar radiation and moisture availability, and slope has a strong influence on fire intensity. Our study corroborated these conclusions: areas showing a high burn severity level were located in a relatively flat high plateau, so elevation was the topographic covariate that most contributed to model high burn severity. However, moderate and low burn severities were mainly found in canyons with north-east and south-east aspects, thus AS was the relevant topographic covariate in these burn severity levels.

We did not use weather-related variables in our study, however different studies have shown the impact of weather conditions on burn severity (e.g. Estes et al., 2017; Kane et al., 2015). Particularly Bessie and Johnson (1995) and Estes et al. (2017), indicated that environmental factors (e.g., weather conditions and topography) have

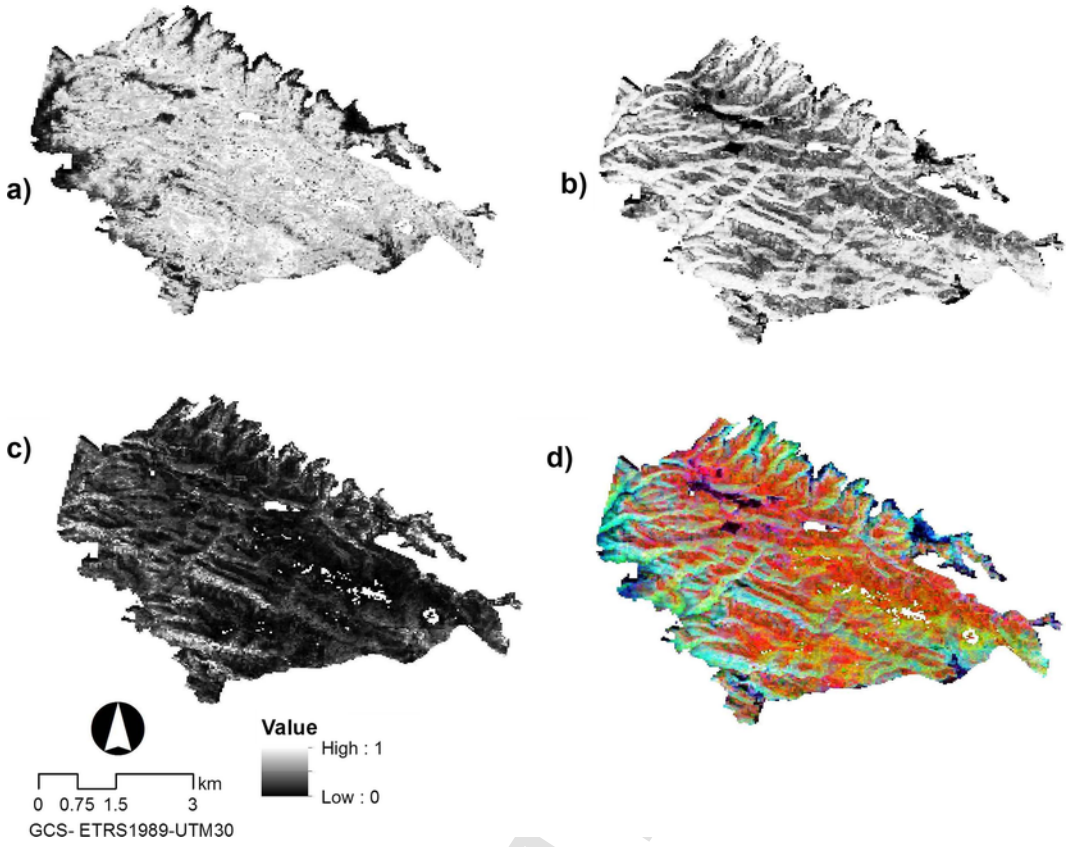

Fig. 5. a) Suitability surface of high burn severity level; b) Suitability surface of moderate severity level; c) Suitability surface of low burn severity level, d) False color composition RGB: high:moderate:low.

more importance on fire severity than fuels. Conversely Lentile et al. (2006) and Lydersen et al. (2017) showed a clear relationship between burn severity and fuels. The inclusion of weather conditions as potential drivers of burn severity will be examined in a future work.

In our study, Maxent built three probability images (low, moderate and high burn severity) from which it is possible to produce different specific maps depending the specific goals and needs. From them it was shown that the central and southern part of burned area corresponded mainly with high burn severity, moderate burn severity areas were located mostly in canyons near of fire perimeter, and there were very few areas classified as low burn severity level, which agrees with the burn severity pattern of Carcaixent Fire in 2016. The most useful information for forest managers might be the continuous suitability surfaces (probability of occurrence maps) because they enable us to adjust the threshold to the project priorities (Vogeler et al., 2016). Thus, the fact of having available probability of occurrence maps represents one advantage of MaxEnt vs. conventional hard classifiers. Moreover, as fraction images have a physical meaning (the abundance of each endmember within the pixel) the interpretation of their contribution in the MaxEnt final model is not complicated. Morgan et al. (2014) and Veraverbeke and Hook (2013) among others have already highlighted the benefit of this relationship between fraction images and field proportions. In fact, the combination of MESMA fraction images, LiDAR-derived metrics and MaxEnt provided a physical meaning to the complete model process, easing its use and comprehension.

Summarizing, the different features of our proposed method to model burn severity is based on the following facts: 1) fraction images were chosen to represent the post-fire vegetation damage instead of spectral indices. The reason of this decision was twofold: a) we kept all reflectance band information (as contrasted with spectral indices that only use information from two/three spectral bands) and thus burned vegetation may be more accurately characterized and b) we could reduce the influence of background soil; 2) MESMA, which has been found to be superior to simple SMA, was selected to perform unmixing and obtain the fraction images; 3) our study was based on hyperspectral data instead of multispectral imagery. Some studies (Veraverbeke et al., 2014, 2018) pointed out the advantages of hyperspectral vs. multispectral data to assess fire severity: mainly its higher data dimensionality and also their narrowbands; 4) It is a quasi-multitemporal method where the pre-fire data were not hyper-/multi-spectral imagery but LiDAR data. Thus, it could avoid the selection and correction of pre-fire image without losing the pre-fire vegetation information; 5) MaxEnt is a powerful one-class classifier that provides continuous probability of occurrence maps instead of just a discrete quantification of post-fire damage of vegetation; and 6) the described burn severity modeling method may be appropriated for different ecosystems (Mediterranean and non-Mediterranean). MESMA produces accurate fraction images in every ecosystem if candidate endmembers are selected adequately and careful from the image. Finally, MaxEnt is a one-class classifier that no needs any ecosystem specific parameter to work properly. Our work represents a novel approach whose conclusions should be tested in more fire events, with different characteristics (fire regime, weather, topography, …). However, we believe that it may be a reference to be compared with the results of new studies. Although we used only a fire, it was relatively large. It was the second largest fire in Spain in 2016 (San-Miguel-Ayanz et al., 2016).

7. Conclusion

We verified a quasi-multitemporal method based on post-fire hyperspectral data and complemented by pre-fire LiDAR that modeled accurately three levels of burn severity. In addition the use of a one-class classifier, MaxEnt, allowed us to analyze the contribution of each taken

into account covariate in each of the three burn severity levels. Information from EO-1 Hyperion data was extracted by using MESMA, being the char fraction image who most contributed to the final model of every burn severity level. A careful and structured spectral library building (char, GV, NPVS) including all land covers under study was an indispensable requirement to obtain the needed accurate fraction images. Pre-fire LiDAR-derived metrics were classified into two groups: 1) parameters that define the vertical structure of vegetation. Their global contribution was similar for high and moderate burn severity but their contribution increased in the low burn severity level reaching 16.28%, and 2) parameters that define the horizontal structure whose influence was relatively low on the high burn severity level and relatively high on the low burn severity level (8.55%). Topographic DEM-derived parameters were also taken into account in the final model. Their percentage of contribution to the final model was similar for the three burn severity levels (approximately 20%). Our results proved that burn severity levels can be modeled from MaxEnt trained using post-fire MESMA Hyperion fraction images, and pre-fire LiDAR-derived variables (research question 1) with MESMA char fraction contributing between 54.45% for low burn severity level and 73.86% for high burn severity one, and LiDAR-derived metrics between 24.83% for low and 7.43% for high burn severity level (research question 2). We corroborated the potential of LiDAR data to describe vegetation structure and fuel loads, as they provided structural information about pre-fire vegetation in our final MaxEnt model in adverse conditions from a technical point of view: low density LiDAR data and predominance of low and dense vegetation (bushes). Though sharing a trend pattern, each burn severity level had its own modeling structure. For low burn severity level the contribution of LiDAR data was a relatively high, whereas the contribution of char fraction decreased, whereas for high burn severity level the contribution of LiDAR–derived metrics was relatively low while char fraction gained in importance (research question 3).

The proposed method may contribute to improve the analysis of burn severity patterns and take adequate post-fire management decisions. This methodology might be easily extrapolated to different ecosystems (Mediterranean and non-Mediterranean), in spite that our study area is situated in a Mediterranean region. Thus, our study presents a new methodology which takes advantage of a new generation of spaceborne hyperspectral missions (like the Hyperspectral Infrared Imager, HyspIRI, the Environmental Mapping And Analysis Program, EnMAP, and the Precursore Iperspettrale Della Missione Applicativa, PRISMA), and improved availability of LiDAR data (in particular, the Global Ecosystem Dynamics Investigation –GEDI- full-waveform LiDAR recently deployed on the International Space Station (ISS) in 2018 for a two-year mission) to evaluate post-fire effects on vegetation using the powerful one-class classifier MaxEnt.

Uncited references

Cao et al. (2013), Congalton and Green (2009), Drake et al. (1999), Eckmann et al. (2008), Elith et al. (2006), Jaynes (1990), Lezberg et al. (2008), Meng et al. (2017), Merow et al. (2013), Miler and Thode (2007), Nenzen and Araujo (2011), Phillips et al. (2009), Rothermel (1983).

Acknowledgments

The Spanish Ministry of Economy and Competitiveness funded this study (FIRESEVES project, AGL2017-86075-C2-1-R), and the Regional Government of Castile and León (SEFIRECYL project, LE001P17). The two first authors obtained two Spanish Education Ministry grants (Salvador de Madariaga program, codes PRX17/00234 and PRX17/00133) to visit the VIPER Lab. (University of California, Santa Barbara). The authors thank Juan José Peón García from University of Oviedo (Spain) for helping with image acquisition request and Generalitat Valenciana (Autonomous Government) for providing official Carcaixent Fire information

References

AEMET-IM, 2011. AEMET-IM, 2011. Iberian Climate Atlas. Air temperature and precipitation (1971–2000). Agencia Estatal de Meteorología, Ministerio de Medio Ambiente y Medio Rural y Marino. Instituto de Meteorologia de Portugal.

Agee, J.K., 1997. The severe weather wildfire: too hot to handle?. Northwest Sci. 71, 153–156.

Agee, J.K., Skinner, C.N., 2005. Basic principles of forest fuel reduction treatments. For. Ecol. Manage. 211, 83–96.

Ahmed, O.S., Franklin, S.E., Wulder, M.A., White, J.C., 2015. Characterizing stand-level forest canopy cover and height using Landsat time series, samples of airborne LiDAR, and the Random Forest algorithm. ISPRS J. Photogramm. Remote Sens. 101, 89–101.

Alonzo, M., Roth, K., Roberts, D.A., 2013. Identifying Santa Barbara's urban tree species from AVIRIS imagery using canonical discriminant analysis. Remote Sens. Lett. 4 (5), 513–521.

Alonzo, M., Bookhagen, B., Roberts, D.A., 2014. Urban tree species mapping using hyperspectral and lidar data fusion. Remote Sens. Environ. 148, 70–83.

Amaral, C.H., Roberts, D.A., Almeida, T.I.R., Souza-Filho, C.R., 2015. Mapping invasive species and spectral mixture relationships with neotropical woody formations in southeastern Brazil. ISPRS J. Photogramm. Remote Sens. 108, 80–93.

Amici, V., Marcantonio, M., La Porta, N., Rocchini, D., 2017. A multi-temporal approach in MaxEnt modelling: A new frontier for land use/land cover change detection. Ecol. Inf. 40, 40–49.

Arnold, J.D., Brewer, S.C., Dennison, P.E., 2014. Modeling climate-fire connections within the Great basin and Upper Colorado river basin, Western United State. Fire Ecol. 10, 64–75.

Arpaci, A., Malowerschnig, B., Sass, O., Vacik, H., 2014. Using multi variate data mining techniques for estimating fire susceptibility of Tyrolean forests. Appl. Geogr. 53, 258e270.

Baker, W.L., 2014. Historical forest structure and fire in Sierran mixed-conifer forests reconstructed from General Land Office survey data. Ecosphere 5 (7), 79.

Baldwin, R.B., 2009. Use of maximum entropy modeling in wildlife research. Entropy 11, 854–866.

Berk et al., 1989 Berk, A., Bernstein, L.S., Robertson, D.C., 1989. MODTRAN: a moderate resolution model for LOWTRAN7. GL-TR-89-0122. Air Force Geophysical Laboratory, Hanscom AFB, MA. p. 38.

Bessie, W.C., Johnson, E.A., 1995. The relative importance of fuels and weather on fire behavior in subalpine forests. Ecology 76 (3), 747–762.

Bolton, D.K., Coops, N.C., Wulder, M.A., 2015. Characterizing residual structure and forest recovery following high-severity fire in the western boreal of Canada using Landsat time-series and airborne lidar data. Remote Sens. Environ. 163, 48–60.

Botella-Martínez, M.A., Fernández-Manso, A., 2017. Study of post-fire severity in the Valencia region comparing the NBR, RdNBR and RBR indexes derived from Landsat 8 images. Spanish J. Remote Sens./Revista de Teledetección (RAET) 49, 33–47.

Bowman, D.M.J.S., Balch, J.K., Artaxo, P., Bond, W.J., Carlson, J.M., Cochrane, M.A., D'Antonio, C.M., Defries, R.S., Doyle, J.C., Harrison, S.P., Johnston, F.H., Keeley, J.E., Krawchuk, M.A., Kull, C.A., Marston, J.B., Moritz, M.A., Prentice, I.C., Roos, C.I., Scott, A.C., Swetnam, T.W., van der Werf, G.R., Pyne, S.J., 2009. Fire in the earth system. Science 324, 481–548.

Bradley, A.P., 1997. The use of the area under the ROC curve in the evaluation of machine learning algorithms. Pattern Recogn. 30, 1145–1159.

Brewer, J.S., 2016. Natural canopy damage and the ecological restoration of fire-indicative groundcover vegetation in an oak-pine forest. Fire Ecol. 105–126.

Broncano, M.J., Retana, J., 2004. Topography and forest composition affecting the variability in fire severity and post-fire regeneration occurring after a large fire in the Mediterranean basin. Int. J. Wildland Fire 13 (2), 209–216.

Campbell, 2016 Campbell, D., 2016. The campbell prediction system: a wild land fire prediction system communication system. Fourth ed.

Cao, L., Coops, N.C., Sun, Y., Ruan, H., Wang, G., Dai, J., She, G., 2019. Estimating canopy structure and biomass in bamboo forests using airborne LiDAR data. ISPRS J. Photogramm. Remote Sens. 148, 114–129.

Cao, Y., DeWalt, R.E., Robinson, J.L., Tweddale, T., Hinz, L., Pessino, M., 2013. Using Maxent to model the historic distributions of stonefly species in Illinois streams: The effects of regularization and threshold selections. Ecol. Model. 259, 30–39.

Chen, F., Du, Y., Niu, S., Zhao, J., 2015. Modeling Forest Lightning Fire Occurrence in the Daxinganling Mountains of Northeastern China with MAXENT. Forests 6, 1422–1438.

Chen, G., Metz, M.R., Rizzo, D.M., Dillon, W.W., Meentemeyer, R.K., 2015. Object-based assessment of burn severity in diseased forests using high-spatial and high-spectral resolution MASTER airborne imagery. ISPRS J. Photogramm. Remote Sens. 102, 38–47.

Chen, Y., Zhu, X., Yebra, M., Harris, S., Tapper, N., 2017. Development of a predictive model for estimating forest surface fuel load in Australian eucalypt forests with LiDAR data. Environ. Modell. Software 97, 61–71.

Congalton, R.G., Green, K., 2009. Assessing the accuracy of remotely sensed data Principles and practices, 2nd ed. CRC Press. Taylor & Francis, Boca Raton.

de Angelis, A., Ricotta, C., Conedera, M., Pezzatti, G.B., 2015. Modelling the meteorological forest fire niche in heterogeneous pyrologic conditions. PLoS ONE 10 (2). doi:10.1371/ journal.pone.0116875, e0116875.

della Pietra, S., della Pietra, V., Lafferty, J., 1997. Inducing features of random fields. IEEE Trans. Pattern Anal. Mach. Intell. 19, 1–13.

Dennison, P.E., Roberts, D.A., 2003. Endmember selection for mapping chaparral species and fraction using Multiple Endmember Spectral Mixture Analysis. Remote Sens. Environ. 41, 123–135.
Dennison, P.E., Halligan, K.Q., Roberts, D.A., 2004. A comparison of error metrics and constraints for Multiple Endmember Spectral Mixture Analysis and Spectral Angle Mapper. Remote Sens. Environ. 93, 359–367.
Dennison, P.E., Charoensiri, K., Roberts, D.A., Peterson, S.H., Green, R.O., 2006. Wildfire temperature and land cover modeling using hyperspectral data. Remote Sens. Environ. 100, 212–222.
Drake, N.A., Mackin, S., Settle, J.J., 1999. Mapping vegetation, soils, and geology in semiarid shrublands using spectral matching and mixture modeling of SWIR AVIRIS imagery. Remote Sens. Environ. 68, 12–25.
Dudík and Phillips, 2009 Dudík, M., Phillips, S. 2009. Generative and discriminative learning with unknown labeling bias. – Advances on Neural Information Processing Systems, 21, 1–8.
Dudík et al., 2004 Dudík, M., Phillips, S., Schapire, R.E. 2004. Performance Guarantees for Regularized Maximum Entropy Density Estimation. In: Proceedings of the 17th Annual Conference on Computational Learning Theory.
Dudley, K.L., Dennison, P.E., Roth, K.L., Roberts, D.A., Coates, A.R., 2015. A multi-temporal spectral library approach for mapping vegetation species across spatial and temporal phenological gradients. Remote Sens. Environ. 167, 121–134.
Eckmann, T.C., Roberts, D.A., Still, C.J., 2008. Using multiple endmember spectral mixture analysis to retrieve subpixel fire properties from MODIS. Remote Sens. Environ. 112, 3773–3783.
Elith, J., Graham, C.H., 2009. Do they? How do they? WHY do they differ? On finding reasons for differing performances of species distribution models. Ecography 32, 66–77.
Elith, J., Graham, C.H., Anderson, R.P., Dudik, M., Ferrier, S., Guisan, A., Hijmans, R.J., Huettmann, F., Leathwick, J.R., Lehmann, A., Li, J., Lohmann, L.G., Loiselle, B.A., Manion, G., Moritz, C., Nakamura, M., Nakazawa, Y., Overton, J.M., Peterson, A.T., Phillips, S.J., Richardson, K., Scachetti-Pereira, R., Schapire, R.E., Soberon, J., Williams, S., Wisz, M.S., Zimmermann, N.E., 2006. Novel methods improve prediction of species' distributions from occurrence data. Ecography 29, 129–151.
Elith, J., Phillips, S.J., Hastie, T., Dudík, M., Chee, Y.E., Yates, C.J., 2011. A statistical explanation of MaxEnt for ecologists. Divers. Distrib. 17, 43–57.
EO-1 User Guide, 2003 EO-1 User Guide. Version 2.3. 2003. Satellite Systems Branch USGS Earth Resources Observation Systems Data Center (EDC). Compiled by Beck. R. (http://eo1.usgs.gov and http://eo1.gsfc.nasa.gov).
Erdody, T.L., Moskal, L.M., 2010. Fusion of LiDAR and imagery for estimating forest canopy fuels. Remote Sens. Environ. 114, 725–737.
Estes, B.L., Knapp, E.E., Skinner, C.N., Miller, J.D., Preisler, H.K., 2017. Factors influencing fire severity under moderate burning conditions in the Klamath Mountains, northern California, USA. Ecosphere 8, e01794.
Estornell, J., Ruiz, L.A., Velazquez-Marti, B., 2011. Study of shrub cover and height using LIDAR data in a Mediterranean area. For. Sci. 57, 171–179.
Fawcett, T., 2006. An introduction to ROC analysis. Pattern Recogn. Lett. 27, 861–874.
Felicísimo, A., Cuartero, A., Remondo, J., Quiros, E., 2012. Mapping landslide susceptibility with logistic regression, multiple adaptive regression splines, classification and regression trees, and maximum entropy methods: a comparative study. Landslides 9, 175–189.
Fernandes, P.M., Rigolot, E., 2007. The fire ecology and management of maritime pine (Pinus pinaster Ait.). For. Ecol. Manage. 241, 1–13.
Fernández-Manso, A., Quintano, C., Roberts, D., 2012. Evaluation of potential of multiple endmember spectral mixture analysis (MESMA) for surface coal mining affected area mapping in different world forest ecosystems. Remote Sens. Environ. 127, 181–193.
Fernández-García, V., Santamarta, M., Fernández-Manso, A., Quintano, C., Marcos, E., Calvo, L., 2018. Burn severity metrics in fire-prone pine ecosystems along a climatic gradient using Landsat imagery. Remote Sens. Environ. 206, 205–217.
Fernández-Manso, A., Fernandez-Manso, O., Quintano, C., 2016. SENTINEL-2A red-edge spectral indices suitability for discriminating burn severity. Int. J. Appl. Earth Obs. Geoinf. 50, 170–175.
Fernández-Manso, A., Quintano, C., Roberts, D.A., 2016. Burn severity influence on post-fire vegetation cover resilience from Landsat MESMA fraction images time series in Mediterranean forest ecosystems. Remote Sens. Environ. 184, 112–123.
Fernández-Manso, O., Quintano, C., Fernández-Manso, A., 2009. Combining spectral mixture analysis and object-based classification for fire severity mapping. For. Syst. 18, 296–313.
Fonseca, M.G., Aragao, L.E.O.C., Lima, A., Shimabukuro, Y.E., Arai, E., Anderson, L.O., 2016. Modelling fire probability in the Brazilian Amazon using the maximum entropy method. Int. J. Wildland Fire 25, 955–969.
Fonseca, M.G., Anderson, L.O., Arai, E., Shimabukuro, Y.E., Xaud, H.A.M., Xaud, M.R., Madani, N., Wagner, F.H., Aragao, L.E.O.C., 2017. Climatic and anthropogenic drivers of northern Amazon fires during the 2015–2016 El Niño event. Ecol. Appl. 27, 2514–2527.
Forest Fires Prevention Service (FFPS), 2016 Forest Fires Prevention Service (FFPS). 2016. Carcaixent Postfire Report. Ministry of Agriculture, Environment, Climate Change and Rural Development.
Franke, J., Roberts, D.A., Halligan, K., Menz, G., 2009. Hierarchical multiple endmember spectral mixture analysis (MESMA) of hyperspectral imagery for urban environments. Remote Sens. Environ. 113, 1712–1723.
Frolking, S., Palace, M.W., Clark, D.B., Chambers, J.Q., Shugart, H.H., Hurtt, G.C., 2009. Forest disturbance and recovery: a general review in the context of spaceborne remote sensing of impacts on aboveground biomass and canopy structure. J. Geophys. Res. Biogeosci. 114, G00E02.
García-Llamas, P., Suárez-Seoane, S., Taboada, A., Marcos, E., Fernández-Manso, A., Quintano, C., Fernández-García, V., Fernández-Guisuraga, J.M., Calvo, L., 2019. Environmental drivers of fire severity in extreme fire events that affect Mediterranean pine forest ecosystems. For. Ecol. Manage. 433, 24–32.
George, R., Padalia, H., Kushwaha, S.P.S., 2014. Forest tree species discrimination in western Himalaya using EO-1 Hyperion. Int. J. Appl. Earth Obs. Geoinf. 28, 140–149.
Gill, N.S., Sangermano, F., Buma, B., Kulakowski, D., 2017. Populus tremuloides seedling establishment: An underexplored vector for forest type conversion after multiple disturbances. For. Ecol. Manage. 404, 156–164.
Giovannini, A., Seglie, D., Giacoma, C., 2014. Identifying priority areas for conservation of spadefoot toad, Pelobates fuscus insubricus using a maximum entropy approach. Biodivers. Conserv. 23, 1427–1439.
Green, R.O., Eastwood, M.L., Sarture, C.M., Chrien, T.G., Aronsson, M., Chippendale, B.J., Faust, J.A., Pavri, B.E., Chovit, C.J., Solis, M., Olah, M.R., Williams, O., 1998. Imaging spectroscopy and the airborne visible/infrared imaging spectrometer (AVIRIS). Remote Sens. Environ. 65, 227–248.
Gu, C., Clevers, J.G.P.W., Liu, X., Tian, X., Li, Z., Li, Z., 2018. Predicting forest height using the GOST, Landsat 7 ETM+, and airborne LiDAR for sloping terrains in the Greater Khingan Mountains of China. ISPRS J. Photogramm. Remote Sens. 137, 97–111.
Hamada, Y., Stow, D.A., Roberts, D.A., 2011. Estimating life-form cover fractions in California sage scrub communities using multispectral remote sensing. Remote Sens. Environ. 115, 3056–3068.
Harris, L., Taylor, A.H., 2015. Topography, fuels, and fire exclusion drive fire severity of the Rim Fire in an old-growth mixed-conifer forest, Yosemite Natioanl Park, USA. Ecosystems 18, 1192–1208.
Hastie et al., 2009 Hastie, T.J., Tibshirani, R.J., Friedman, J., 2009. The elements of statistical learning. Dordrecht, editor: Springer.
Heyerdahl, E.K., Brubaker, L.B., Agee, J.K., 2001. Spatial controls of historical fire regimes: a multiscale example from the interior West, USA. Ecology 82, 660–678.
Huang, S., Jin, S., Dahal, D., Chen, X., Young, C., Liu, H., Liu, S., 2013. Reconstructing satellite images to quantify spatially explicit land surface change caused by fires and succession: A demonstration in the Yukon River Basin of interior Alaska. ISPRS J. Photogramm. Remote Sens. 79, 94–105.
Hudak, A., Morgan, P., Bobbitt, M., Smith, A., Lewis, S., Lentile, L., Robichaud, P., Clark, J., McKinley, R., 2007. The relationship of multispectral satellite imagery to immediate fire effects. Fire Ecol. 3, 64–90.
Jain, T.B., Pilliod, D., Graham, R.T., 2004. Tongue-tied. Confused meanings for common fire terminology can lead to fuels mismanagement. A new framework is needed to clarify and communicate the concepts. Wildfire 4, 22–26.
Jaynes, E.T., 1957. Information theory and statistical mechanics. Phys. Rev. 106, 620–630.

Jaynes, E.T., 1990. Notes on present status and future prospects. In: Grandy, W.T., Schick, L.H. (Eds.), Maximum Entropy and Bayesian Methods, Kluwer, Dordrecht, The Netherlands, pp. 1–13.
Jones, C., Song, C., Moody, A., 2015. Where's woolly? An integrative use of remote sensing to improve predictions of the spatial distribution of an invasive forest pest the Hemlock Woolly Adelgid. For. Ecol. Manage. 358, 222–229.
Kane, V.R., Cansler, C.A., Povak, N.A., Kane, J.T., McGaughey, R.J., Lutz, J.A., Churchill, D.J., North, M.P., 2015. Mixed severity fire effects within the Rim fire: Relative importance of local climate, fire weather, topography, and forest structure. For. Ecol. Manage. 358, 62–79.
Kane et al., 2014a — Kane, V.R., Kopper, K., Copass, C., 2014a. Mapping the Fuel Characteristics of Mount Rainier National Park: A fusion of field, environmental and LiDAR data. Final Report to the National Park Service.
Kane, V.R., Lutz, J.A., Roberts, S.L., Smith, D.F., McGaughey, R.J., Povak, N.A., Brooks, M.L., 2013. Landscape-scale effects of fire severity on mixed-conifer and red fir forest structure in Yosemite National Park. For. Ecol. Manage. 287, 17–31.
Kane, V.R., North, M.P., Lutz, J.A., Churchill, D.J., Roberts, S.L., Smith, D.F., McGaughey, R.J., Kane, J.T., Brooks, M.L., 2014. Assessing fire effects on forest spatial structure using a fusion of Landsat and airborne LiDAR data in Yosemite National Park. Remote Sens. Environ. 151, 89–101.
Keane, R.E., Burgan, R., van Wagtendonk, J., 2001. Mapping wildland fuels for fire management across multiple scales: integrating remote sensing, GIS, and biophysical modelling. Int. J. Wildland Fire 10, 301–319.
Keeley, J.E., 2009. Fire intensity, fire severity and burn severity: A brief review and suggested usage. Int. J. Wildland Fire 18, 116–126.
Key and Benson, 2006 — Key, C.H., Benson, N.C., 2006. Landscape assessment (LA). Sampling and analysis methods. USDA Forest Service Gen. Tech. Rep. RMRS-GTR-164-CD.
Kramer, H.A., Collins, B.M., Kelly, M., Stephens, S.L., 2014. Quantifying ladder fuels: a new approach using LiDAR. Forests 5, 1432–1453.
Kuenzi, A.M., Fulé, P.Z., Sieg, C.H., 2008. Effects of fire severity and pre-fire stand treatment on plant community recovery after a large wildfire. For. Ecol. Manage. 255, 855–865.
Lentile, L., Holden, Z., Smith, A., Falkowski, M., Hudak, A., Morgan, P., Lewis, S., Gessler, P., Benson, N., 2006. Remote sensing techniques to assess active fire characteristics and post-fire effects. Int. J. Wildland Fire 15, 319–345.
Lentile, L., Smith, A., Hudak, A., Morgan, P., Bobbitt, M., Lewis, S., Robichaud, P., 2009. Remote sensing for prediction of 1-year post-fire ecosystem condition. Int. J. Wildland Fire 18, 594–608.
Lezberg, A.L., Battaglia, M.A., Shepperd, W.D., Schoettle, A.W., 2008. Decades-old silvicultural treatments influence surface wildfire severity and post-fire nitrogen availability in a ponderosa pine forest. For. Ecol. Manage. 255 (1), 49–61.
Lhermitte, S., Verbesselt, J., Verstraeten, W.W., Veraverbeke, S., Coppin, P., 2011. Assessing intra-annual vegetation regrowth after fire using the pixel based regeneration index. ISPRS J. Photogramm. Remote Sens. 66, 17–27.
Li, W., Guo, Q., 2010. A maximum entropy approach to oneclass classification of remote sensing imagery. Int. J. Remote Sens. 31 (8), 2227–2235.
Lin, J., Liu, X., Li, K., Li, X., 2014. A maximum entropy method to extract urban land by combining MODIS reflectance, MODIS NDVI, and DMSP-OLS data. Int. J. Remote Sens. 35, 6708–6727.
Lippitt, C.L., Stow, D.A., Roberts, D.A., Coulter, L.L., 2017. Multidate MESMA for monitoring vegetation growth forms in southern California shrublands. Int. J. Remote Sens. 39, 655–683.
Liu, K., Shen, X., Cao, L., Wang, G., Cao, F., 2018. Estimating forest structural attributes using UAV-LiDAR data in Ginkgo plantations. ISPRS J. Photogramm. Remote Sens. 146, 465–482.
Lu, B., He, Y., Tong, A., 2015. Evaluation of spectral indices for estimating burn severity in semiarid grasslands. Int. J. Wildland Fire 25, 147–157.
Lydersen, J.M., Collins, B.M., Brooks, M.L., Matchett, J.R., Shive, K.L., Povak, N.A., Kane, V.R., Smith, D.F., 2017. Evidence of fuels management and fire weather influencing fire severity in an extreme fire event. Ecol. Appl. 27, 2013–2030.
Lydersen, J.M., North, M.P., Collins, B.M., 2014. Severity of an uncharacteristically large wildfire, the Rim Fire, in forests with relatively restored frequent fire regimes. For. Ecol. Manage. 328, 326–334.
Marino, E., Montes, F., Tomé, J.L., Navarro, J.A., Hernando, C., 2018. Vertical forest structure analysis for wildfire prevention: Comparing airborne laser scanning data and stereoscopic hemispherical images. Int. J. Appl. Earth Obs. Geoinf. 73, 438–449.
Marino, E., Ranz, P., Tomé, J.L., Noriega, M.A., Esteban, J., Madrigal, J., 2016. Generation of high-resolution fuel model maps from discrete airborne laser scanner and Landsat-8 OLI: A low-cost and highly updated methodology for large areas. Remote Sens. Environ. 187, 267–280.
Matthew, M.W., Adler-Golden, S.M., Berk, A., Richtsmeier, S.C., Levine, R.Y., Bernstein, L.S., Acharya, P.K., Anderson, G.P., Felde, G.W., Hoke, M.P., Ratkowski, A., Burke, H.-H., Kaiser, R.D., Miller, D.P., 2000. Status of Atmospheric Correction Using a MODTRAN4-based Algorithm. SPIE Proceedings, Algorithms for Multispectral, Hyperspectral, and Ultraspectral Imagery VI. 4049, 199–207.
McCarley, T.R., Kolden, C.A., Vaillant, N.M., Hudak, A.T., Smith, A.M.S., Wing, B.M., Kellogg, B.S., Kreitler, J., 2017. Multi-temporal LiDAR and Landsat quantification of fire-induced changes to forest structure. Remote Sens. Environ. 191, 419–432.
McGaughey, 2018 — McGaughey, R.J., 2018. FUSION/LDV: Software for LiDAR data analysis and visualization version 3.70
Meng, R., Zhao, F., 2017. A review for recent advances in burned area and burn severity mapping. In: Petropoulos, G.P., Islam, T. (Eds.), Remote Sensing of Hydrometeorological Hazards, Taylor & Francis.
Meng, R., Wu, J., Schwager, K.L., Zhao, F., Serbin, S.P., 2017. Using high spatial resolution satellite imagery to map forest burn severity across spatial scales in a Pine Barrens ecosystem. Remote Sens. Environ. 191, 95–109.
Merow, C., Smith, M.J., Silander, J.A., Jr, 2013. A practical guide to MaxEnt for modeling species' distributions: what it does, and why inputs and settings matter. Ecography 36, 1058–1069.
Miler, J.D., Thode, A.E., 2007. Quantifying burn severity in a heterogeneous landscape with a relative version of the delta Normalized Burn Ratio (dNBR). Remote Sens. Environ. 109, 66–80.
Michishita, R., Jiang, Z., Gong, P., Xu, B., 2012. Bi-scale analysis of multitemporal land cover fractions for wetland vegetation mapping. ISPRS J. Photogramm. Remote Sens. 72, 1–15.
Montealegre, A.L., Lamelas, M.T., Tanase, M.A., de la Riva, J., 2014. Forest fire severity assessment using ALS data in a mediterranean environment. Remote Sens. 6, 4240–4265.
Monterroso, P., Brito, J.C., Ferreras, P., Alves, P.C., 2009. Spatial ecology of the European wildcat in a Mediterranean ecosystem: dealing with small radio-tracking datasets in species conservation. J. Zool. 279, 27–35.
Morgan, P., Keane, R.E., Dillon, G.K., Jain, T.B., Hudak, A.T., Karau, E.C., Sikkink, P.G., Holden, Z.A., Strand, E.K., 2014. Challenges of assessing fire and burn severity using field measures, remote sensing and modeling. Int. J. Wildland Fire 23, 1045–1060.
Mutlu, M., Popescu, S.C., Stripling, C., Spencer, T., 2008. Mapping surface fuel models using LiDAR and multispectral data fusion for fire behavior. Remote Sens. Environ. 112, 274–285.
Mutlu, M., Popescu, S.C., Zhao, K., 2008. Sensitivity analysis of fire behavior modeling with LiDAR-derived surface fuel maps. For. Ecol. Manage. 256, 289–294.
Naidoo, L., Cho, M.A., Mathieu, R., Asner, G., 2012. Classification of savanna tree species, in the Greater Kruger National Park region, by integrating hyperspectral and LiDAR data in a Random Forest data mining environment. ISPRS J. Photogramm. Remote Sens. 69, 167–179.
Nenzen, H.K., Araujo, M.B., 2011. Choice of threshold alters projections of species range shifts under climate change. Ecol. Modeling 222, 3346–3354.
O'Connor, C.D., Calkin, D.E., Thompson, M.P., 2017. An empirical machine learning method for predicting potential fire control locations for pre-fire planning and operational fire management. Int. J. Wildland Fire 26, 587–597.
Parisien, M., Moritz, M.A., 2009. Environmental controls on the distribution of wildfire at multiple spatial scales. Ecol. Monogr. 79, 127–154.
Parisien, M., Snetsinger, S., Greenberg, J.A., Nelson, C.R., Schoennagel, T., Dobrowski, S.Z., Moritz, M.A., 2012. Spatial variability in wildfire probability across the western United States. Int. J. Wildland Fire 12, 313–327.
Park, N.-W., 2015. Using maximum entropy modeling for landslide susceptibility mapping with multiple geoenvironmental data sets. Environ. Earth Sci. 73, 937–949.

Parker, G.G., Russ, M.E., 2004. The canopy surface and stand development: assessing forest canopy structure and complexity with near-surface altimetry. For. Ecol. Manage. 189, 307–315.
Parsons, A., Robichaud, P.R., Lewis, S.A., Napper, C., Clark, J., Jain, T.B., 2010. Field guide for mapping post-fire soil burn severity. Water October, 49.
Pearlman, J.S., Barry, P.S., Segal, C.C., Shepanski, J., Beiso, D., Carman, S.L., 2003. Hyperion, a space-based imaging spectrometer. IEEE Trans. Geosci. Remote Sens. 41, 1160–1173.
Peters, M.P., Iverson, L.R., Matthews, S.N., Prasad, A.M., 2013. Wildfire hazard mapping exploring site conditions in eastern US wildland-urban interfaces. Int. J. Wildland Fire 22, 567–578.
Phillips et al., 2004 Phillips, S.J., Dudík, M., Schapire, R.E., 2004. A maximum entropy approach to species distribution modeling. In: Proceedings of the Twenty-First International Conference on Machine Learning, 655-662.
Phillips, S.J., Anderson, R.P., Schapire, R.E., 2006. Maximum entropy modeling of species geographic distributions. Ecol. Model. 190, 231–259.
Phillips, S.J., Dudik, M., 2008. Modeling of species distributions with Max-Ent: new extensions and a comprehensive evaluation. Ecography 31, 161–175.
Phillips, S.J., Dudík, M., Elith, J., Graham, C.H., Lehmann, A., Leathwick, J., Ferrier, S., 2009. Sample selection bias and presence-only distribution models: implications for background and pseudo-absence data. Ecol. Appl. 19, 181–197.
Phillips, 2017 Phillips, S. J. 2017. A Brief Tutorial on Maxent. Available from URL: http://biodiversityinformatics.amnh.org/open_source/maxent/. Accessed on 13/05/2018.
Phillips, S.J., Anderson, R.P., Dudík, M., Schapire, R.E., Blair, M., 2017. Opening the black box: an open-source release of Maxent. Ecography 40, 887–893.
Pike, R.J., Wilson, S.E., 1971. Elevation-relief ratio, hypsometric integral, and geomorphic area-altitude analysis. Geol. Soc. Am. Bull. 82, 1079–1084.
Pleniou, M., Koutsias, N., 2013. Sensitivity of spectral reflectance values to different burn and vegetation ratios: A multi-scale approach applied in a fire affected area. ISPRS J. Photogramm. Remote Sens. 79, 199–210.
Price, O.F., Gordon, C.E., 2016. The potential for LiDAR technology to map fire fuel hazard over large areas of Australian forest. J. Environ. Manage. 181, 63e673.
Quintano, C., Fernández-Manso, A., Fernández-Manso, O., 2018. Combination of Landsat and Sentinel-2 MSI data for initial assessing of burn severity. Int. J. Appl. Earth Observ. Geoinform. 64, 221–225.
Quintano, C., Fernández-Manso, A., Roberts, D.A., 2013. Multiple endmember spectral mixture analysis (MESMA) to map burn severity levels from Landsat images in Mediterranean countries. Remote Sens. Environ. 136, 76–88.
Quintano, C., Fernández-Manso, A., Roberts, D.A., 2017. Burn severity mapping from Landsat MESMA fraction images and Land Surface Temperature. Remote Sens. Environ. 190, 83–95.
Quintano, C., Fernández-Manso, A., Shimabukuro, Y.E., Pereira, G., 2012. Spectral unmixing. Int. J. Remote Sens. 33, 5307–5340.
Radosavljevic, A., Anderson, R.P., 2014. Making better Maxent models of species distributions: complexity, overfitting, and evaluation. J. Biogeogr. 41, 629–643.
Rahmati, O., Pourghasemi, H.R., Melesse, A.M., 2016. Application of GIS-based data driven random forest and maximum entropy models for groundwater potential mapping: A case study at Mehran Region. Iran. Catena 137, 360–372.
Renard, Q., Pelissier, R., Ramesh, B.R., Kodandapani, N., 2012. Environmental susceptibility model for predicting forest fire occurrence in the Western Ghats of India. Int. J. Wildland Fire 21, 368–379.
Ricotta, C., Avena, G., De Palma, A., 1999. Mapping and monitoring net primary productivity with AVHRR NDVI time-series: statistical equivalence of cumulative vegetation indices. ISPRS J. Photogramm. Remote Sens. 54, 325–331.
Roberts, D.A., Gardner, M., Church, R., Ustin, S., Scheer, G., Green, R.O., 1998. Mapping chaparral in the Santa Monica Mountains using multiple endmember spectral mixture models. Remote Sens. Environ. 65, 267–279.
Roberts, D.A., Dennison, P.E., Gardner, M., Hetzel, Y., Ustin, S.L., Lee, C., 2003. Evaluation of the potential of Hyperion for fire danger assessment by comparison to the Airborne Visible/Infrared Imaging Spectrometer. IEEE Trans. Geosci. Remote Sens. 41, 1297–1310.
Roberts, D.A., Dennison, P.E., Roth, K.L., Dudley, K., Hulley, G., 2015. Relationships between dominant plant species, fractional cover and land surface temperature in a Mediterranean ecosystem. Remote Sens. Environ. 167, 152–167.
Roberts et al., 2007 Roberts, D.A., Halligan, K., Dennison, P., 2007. VIPER Tools User Manual. V1.5.
Rodríguez-Veiga, P., Saatchi, S., Tansey, K., Balzter, H., 2016. Magnitude, spatial distribution and uncertainty of forest biomass stocks in Mexico. Remote Sens. Environ. 183, 265–281.
Rothermel, 1983 Rothermel, R.C., 1983. How to Predict the Spreads and Intensity of Forest and Range Forest Fires; U.S. Department of Agriculture, Forest Service: Ogden, UT, USA, 1983.
Saatchi, S., Buermann, W., Steege, H., Mori, S., Smith, T.B., 2008. Modeling distribution of Amazonian tree species and diversity using remote sensing measurements. Remote Sens. Environ. 112, 2000–2017.
San-Miguel-Ayanz et al., 2016 San-Miguel-Ayanz, J., Durrant, T., Boca, R., Libertá, G., Branco, A., de Rigo, D., Ferrari, D., Malanti, P., Vivancos, T.A., Schulte, E., Loffler, P., 2017. Forest fires in Europe, Middle East and North Africa 2016. EUR 28707 EN, Publications Office, Luxemburg, ISBN 978-92-79-71292-0.
Sánchez-Sánchez, Y., Martínez-Graña, A., Francés, F.S., Mateos-Picado, M., 2018. Mapping wildfire ignition probability using sentinel 2 and LiDAR (Jerte Valley, Cáceres, Spain). Sensors 18, 826.
Scott, A.C., Bowman, D.M., Bond, W.J., Pyne, S.J., Alexander, M.E., 2013. Fire on Earth: An Introduction, John Wiley & Sons, Chichester, UK.
Scott, J.H., Burgan, R.E., 2005. Standard fire behavior fuel models: a comprehensive set for use with Rothermel's surface fire spread model. Gen. Tech. Rep. RMRS-GTR-153. Fort Collins, CO: U.S. Department of Agriculture. For. Serv., Rocky Mountain Res. Station 72 p.
Shimabukuro, Y.E., Smith, J., 1991. The least-squares mixing models to generatefraction images derived from remote sensing multispectral data. IEEE Trans. Geosci. Remote Sens. 29, 16–21.
Smith, D.M., 1986. The practice of silviculture, John Wiley and Sons Inc, New York, p. 527 pp.
Somers, B., Verbesselt, J., Ampe, E.M., Sims, N., Verstraeten, W.W., Coppin, P., 2010. Spectral mixture analysis to monitor defoliation in mixed-aged Eucalyptus globulus Labill plantations in southern Australia using Landsat 5-TM and EO-1 Hyperion data. Int. J. Appl. Earth Obs. Geoinf. 12, 270–277.
Stavros, E.N., Coen, N., Peterson, B., Singh, H., Schimel, D., 2018. Use of imaging spectroscopy and LIDAR to characterize fuels for fire behavior prediction. Remote Sens. Appl.: Soc. Environ. 11, 41–50.
Stavros, E.N., Tane, Z., Kane, V.R., Veraverbeke, S., McGaughey, R.J., Lutz, J.A., Ramirez, C., 2016. Unprecedented remote sensing data from before and after California King and Rim Megafires. Ecology 97, 3244.
Stroppiana, D., Bordogna, G., Carrara, P., Boschetti, M., Boschetti, L., Brivio, P.A., 2012. A method for extracting burned areas from Landsat TM/ETM + images by soft aggregation of multiple Spectral Indices and a region growing algorithm. ISPRS J. Photogramm. Remote Sens. 69, 88–102.
Sunderman, S.O., Weisberg, P.J., 2011. Remote sensing approaches for reconstructing fire perimeters and burn severity mosaics in desert spring ecosystems. Remote Sens. Environ. 115, 2384–2389.
Swatantran, A., Dubayah, R., Roberts, D., Hofton, M., Blair, J.B., 2011. Mapping biomass and stress in the Sierra Nevada using lidar and hyperspectral data fusion. Remote Sens. Environ. 115, 2917–2930.
Swets, J.A., 1988. Measuring the accuracy of diagnostic systems. Science 240, 1285–1293.
Tane, Z., Roberts, D., Veraverbeke, S., Casas, A., Ramirez, C., Ustin, S., 2018. Evaluating endmember and band selection techniques for multiple endmember spectral mixture analysis using post-fire imaging spectroscopy. Remote Sens. 10, 389.
Tibshirani, R., 1996. Regression shrinkage and selection via the lasso. J. Roy. Stat. Soc. B 58, 267–288.
Tittensor, D.P., Baco, A.R., Brewin, P.E., Clark, M.R., Consalvey, M., Hall-Spencer, J., Rowden, A.A., Schlacher, T., Stocks, K.I., Rogers, A.D., 2009. Predicting global habitat suitability for stony corals on seamounts. J. Biogeogr. 36, 1111–1128.

Tompkins, S., Mustard, J.F., Pieters, C.M., Forsyth, D.W., 1997. Optimization of endmembers for spectral mixture analysis. Remote Sens. Environ. 59, 472–489.
Tracy, J.L., Trabucco, A., Lawing, M., Giermakowski, J.T., Tchakerian, M., Drus, G.M., Coulson, R.N., 2018. Random subset feature selection for ecological niche models of wildfire activity in Western North America. Ecol. Model. 383, 52–68.
Tsui, O.W., Coops, N.C., Wulder, M.A., Marshall, P.L., McCardle, A., 2012. Using multi-frequency radar and discrete-return LiDAR measurements to estimate above-ground biomass and biomass components in a coastal temperate forest. ISPRS J. Photogramm. Remote Sens. 69, 121–133.
Valdecantos, A., Fuentes, D., Alloza, J.A., Vallejo, R., 2016. Report on the impact of the Carcaixent forest fire, CEAM Foundation-Forestry Program.
van Wagtendonk, J.W., Root, R.R., Key, C.H., 2004. Comparison of AVIRIS and Landsat ETM+ detection capabilities for burn severity. Remote Sens. Environ. 92, 397–408.
Veraverbeke, S., Dennison, P., Gitas, I., Hulley, G., Kalashnikova, O., Katagis, T., Kuai, L., Meng, R., Roberts, D., Stavros, N., 2018. Hyperspectral remote sensing of fire: State-of-the-art and future perspectives. Remote Sens. Environ. 216, 105–121.
Veraverbeke, S., Hook, S.J., 2013. Evaluating spectral indices and spectral mixture analysis for assessing fire severity, combustion completeness and carbon emissions. Int. J. Wildland Fire 22, 707–720.
Veraverbeke, S., Hook, S.J., Harris, S., 2012. Synergy of VSWIR (0.4–2.5μm) and MTIR (3.5–12.5μm) data for post-fire assessments. Remote Sens. Environ. 124, 771–779.
Veraverbeke, S., Stavros, E.N., Hook, S.J., 2014. Assessing fire severity using imaging spectroscopy data from the Airborne Visible/Infrared Imaging Spectrometer (AVIRIS) and comparison with multispectral capabilities. Remote Sens. Environ. 154, 153–163.
Vierling, K.T., Swift, C.E., Hudak, A.T., Vogeler, J.C., Vierling, L.A., 2014. How much does the time lag between wildlife field-data collection and LiDAR-data acquisition matter for studies of animal distributions? A case study using bird communities. Geosci. Remote Sens. 5, 185–193.
Vilar, L., Gómez, I., Martínez-Vega, J., Echavarría, P., Riaño, D., Martín, M.P., 2016. Multitemporal modelling of socio-economic wildfire drivers in central spain between the 1980s and the 2000s: comparing generalized linear models to machine learning algorithms. PLoS ONE 11 (8), e0161344.
Vogeler, J.C., Yang, Z., Cohen, W.B., 2016. Mapping post-fire habitat characteristics through the fusion of remote sensing tools. Remote Sens. Environ. 173, 294–303.
Wang, C., Glenn, N.F., 2009. Estimation of fire severity using pre- and post-fire LiDAR data in sagebrush steppe rangelands. Int. J. Wildland Fire 18, 848–856.
Warren, D., Seifert, S., 2011. Ecological niche modeling in MaxEnt: the importance of model complexity and the performance of model selection criteria. Ecol. Appl. 21, 335–342.
Wetherley, E., Roberts, D.A., McFadden, J.P., 2017. Mapping spectrally similar urban materials at sub-pixel scales. Remote Sens. Environ. 195, 170–183.
White and Dieterick, 2012 White, R.A., Dietterick, B.C., 2012. Use of LiDAR and Multispectral Imagery to Determine Conifer Mortality and Burn Severity Following the Lockheed Fire. In: Proceedings of coast redwood forests in a changing California: A symposium for scientists and managers. GENERAL TECHNICAL REPORT PSW-GTR-238. Albany, CA: Pacific Southwest Research Station, Forest Service, U.S. Department of Agriculture. Technical coordinators (Standiford, R.B.; Weller, T. J.; Piirto, D.D.; Stuart, J.D).
Wulder, M.A., White, J.C., Alvarez, F., Han, T., Rogan, J., Hawkes, B., 2009. Characterizing boreal forest wildfire with multi-temporal Landsat and LIDAR data. Remote Sens. Environ. 113, 1540–1555.
Wulder, M.A., White, J.C., Nelson, R.F., Næsset, E., Ørka, H.O., Coops, N.C., Hilker, T., Bater, C.W., Gobakken, T., 2012. Lidar sampling for large-area forest characterization: A review. Remote Sens. Environ. 121, 196–209.
Youngentob, K.N., Roberts, D.A., Held, A.A., Dennison, P.E., Jia, X., Lindenmayer, D.B., 2011. Mapping two Eucalyptus subgenera using multiple endmember spectral mixture analysis and continuum-removed imaging spectrometry data. Remote Sens. Environ. 115, 1115–1128.